ORIGINAL RESEARCH ARTICLE

# $Ag_3Sn$ Morphology Transitions During Eutectic Growth in Sn–Ag Alloys

N. HOU, J.W. XIAN, A. SUGIYAMA, H. YASUDA, and C.M. GOURLAY

Eutectic $Ag_3Sn$ can grow with a variety of morphologies depending on the solidification conditions and plays an important role in the performance of Pb-free solders. Here, we study morphology transitions in the $\beta$-Sn + $Ag_3Sn$ eutectic at increasing growth velocity using a combination of real-time X-ray imaging and analytical electron microscopy. Orthorhombic $Ag_3Sn$ grew as faceted plates or rods with [010] growth direction and (001) as the largest facet in all three eutectic growth morphologies: Irregular plate, broken-lamellar, and rod. Reproducible $\beta$-Sn + $Ag_3Sn$ orientation relationships formed for the latter two morphologies. The mechanisms of spacing adjustment and the reversible transition from plate to rod growth are studied for transient solidification after velocity changes. The transition from fully eutectic growth to $\beta$-Sn dendrites plus eutectic is reasonably reproduced using a competitive growth criterion. At the highest velocities, $Ag_3Sn$ rods developed perturbations whose break down into particles is discussed in terms of unsteady growth and pinch-off mechanisms.

https://doi.org/10.1007/s11661-022-06937-2


## I. INTRODUCTION

$Ag_3Sn$ commonly forms in a eutectic reaction during electronic soldering with Pb-free solders and acts as an important strengthening phase. Increasing the volume fraction of eutectic $Ag_3Sn$ in a solder increases the strength[1,2] and microhardness,[3] and generally improves the thermal fatigue performance of solder joints.[4–6] For a given solder composition, the size, shape, and spacing of eutectic $Ag_3Sn$ play a key role in determining the microhardness[7,8] and the creep rate.[9–12] As a step toward controlling these features, there is a need to better understand the factors affecting the lengthscale and morphology of $Ag_3Sn$ during eutectic solidification, and the competitive growth between $\beta$-Sn dendrites, primary $Ag_3Sn$ plates, and a $\beta$-Sn + $Ag_3Sn$ eutectic front.

The $\beta$-Sn + $Ag_3Sn$ eutectic has been studied intermittently over the last 50 years.[13–18] It is a nonfaceted–faceted (nf–f) eutectic containing a low volume fraction of the faceted $Ag_3Sn$ phase (~ 3.74 vol pct $Ag_3Sn$ at the eutectic composition[19]). Unidirectional solidification experiments (*e.g.*, Bridgman growth), where growth velocity and temperature gradient can be independently controlled, have identified that this eutectic undergoes several morphology transitions with increasing growth rate,[14–16,20] from irregular plate to broken-lamellar and then to rod. Similar transitions occur in other nf–f eutectics with a low volume fraction of the faceted phase including Sn–Zn and Al–$Al_3Ni$.[21] However, there remains significant uncertainty of the factors that determine these transitions in $\beta$-Sn + $Ag_3Sn$. For example, past work has not explored the crystallographic features of these morphology transitions[13–18] which are likely to be significant since this is a nf–f eutectic.[21]

Studies on solder joints[22–26] and cast samples[18,27–30] have reported eutectic $Ag_3Sn$ with the morphology of plates, rods/fibers, and particles/spheroids. The first two are consistent with the unidirectional solidification studies described above but $Ag_3Sn$ particles/spheroids have not been reported in past unidirectional solidification experiments. Therefore, there is a need to better understand the factors affecting the formation of $Ag_3Sn$ particles/spheroids.

It has been shown that the Sn–$Ag_3Sn$ eutectic coupled zone is skewed toward the $Ag_3Sn$ side[17,20] as is common in nf–f eutectics.[31] However, relatively little is known about the competition between dendrites and a eutectic front in this system. For example, the coupled zone has not been calculated, partly due to the requirement to know the undercooling–velocity relationship for the nf–f eutectic, which usually needs to be measured.[32]

N. HOU, J.W. XIAN, and C.M. GOURLAY are with the Department of Materials, Imperial College London, London SW7 2AZ, UK. Contact e-mail: nhou211@gmail.com; c.gourlay@imperial.ac.uk A. SUGIYAMA is with the Department of Mechanical Engineering for Transportation, Osaka Sangyo University, Daito 574-8530, Japan. H. YASUDA is with the Department of Materials Science and Engineering, Kyoto University, Sakyo-ku, Kyoto 606-8501, Japan
Manuscript submitted August 28, 2022; accepted December 12, 2022.
Article published online January 27, 2023

This paper is organized in four parts: (i) the crystallography of growth for each eutectic growth morphology; (ii) the mechanisms by which the morphology transitions and eutectic spacing adjustment occur; (iii) the competition between $\beta$-Sn + $Ag_3Sn$ eutectic growth and $\beta$-Sn dendrite growth; and (iv) the development of $Ag_3Sn$ particles.

## II. METHODS

### A. *Materials*

Sn–x Ag ($x$ = 3.7, 4.0, 4.5, and 5.5 mass percent) alloys, spanning from the eutectic composition to hypereutectic compositions, were selected since the coupled zone is skewed to the side of the faceted phase in nf–f eutectics. The alloys were made by melting 99.99Sn and 99.99Ag in a high-purity graphite crucible and casting. The ingots were rolled into 500 and 50 $\mu$m sheets. Some 500-$\mu$m-thick sheets of Sn–4Ag alloy were also cut into 2 mm × 2 mm square pieces for DSC.

### B. *Unidirectional Solidification Experiments*

Thin sample unidirectional solidification was performed in two types of experiment: by horizontal directional solidification in our laboratory and vertical directional solidification at the SPring-8 synchrotron. Samples for horizontal unidirectional solidification had dimensions 60 mm × 510 mm × 500 $\mu$m. The hot zone was 350 °C and the cold zone was 20.5 °C. The temperature gradient in the liquid near the solid–liquid (S–L) interface was measured to be ~ 12 K/mm in a separate experiment using an immersed 0.25 mm K-type thermocouple. Samples were initially held stationary in the temperature gradient for 30 minutes to partially remelt the alloy and have a stationary $\beta$-Sn + L interface. Unidirectional solidification was then imposed by pulling the sample through the temperature gradient at rates from 0.5 to 500 $\mu$m $s^{-1}$ to a growth distance of about 21 mm. At the end of growth, the growth front was quenched using high pressure room temperature argon gas. In a series of separate directional solidification experiments, the growth temperature of the eutectic front was measured during directional solidification using an embedded thermocouple.

Synchrotron radiography of vertical unidirectional solidification of Sn–3.7Ag alloy was performed on BL20XU at SPring-8 using apparatus developed by Yasuda *et al.*[33]. An energy of 16 keV was applied, and the solidification process was conducted in an argon gas environment. Sn–3.7Ag alloy sheet with dimensions 10 × 10 mm × 50 $\mu$m was placed in a cavity within a 20-$\mu$m-thick PTFE spacer sheet between two $SiO_2$ plates similar to Reference 34. The alloy was initially melted and held for some time until a stationary $\beta$-Sn + L interface was observed. The imaging unit used a phosphor screen and a CMOS camera to record the signal with a field of view of 2048 × 2048 pixels (corresponding to 1 × 1 mm) at 16bit depth. The pixel resolution was 0.502 $\mu$m per pixel and the frame rate was 1 frame per second with 0.5 seconds exposure time. The hot zone was set to 400 °C and the temperature gradient in the liquid near the S–L interface was 6.5 K/mm as measured with a 0.1 mm B-type thermocouple in a separate experiment. After the $\beta$-Sn + L interface was stabilized in the field of view, the sample was pulled downwards away from the hot zone. Pulling velocities in the range 1 to 20 $\mu$m $s^{-1}$ were studied as well as the response of the growth front to velocity changes from/to 1, 10, and 20 $\mu$m $s^{-1}$. Image processing and analysis were performed using Matlab and Image J.[35] Past work on eutectic growth in thin samples and bulk Bridgman-type directional solidification have shown that similar steady state spacings[36] and growth mechanisms[34] are obtained, although thin samples affect the eutectic array configuration.[37]

### C. *Characterization*

Laboratory samples were mounted in Struers Verso-Cit acrylic cold mounting resin and prepared to a colloidal silica finish using standard metallographic procedures. To reveal the three-dimensional (3-D) morphology of the $Ag_3Sn$ phase, some samples were etched in a 60 °C solution of 5 pct NaOH and 3.5 pct ortho-nitrophenol in distilled $H_2O$ by immersion for 3–30 min.

The whole specimen from synchrotron unidirectional solidification was soaked in acetone for a few hours, and the two $SiO_2$ plates were then carefully separated. One $SiO_2$ plate was removed from the specimen and the post solidified thin alloy sample was examined directly without further preparation by analytical SEM. The post-mortem surface microstructure could be correlated with the through-thickness integrated radiographs from the *in situ* image sequence.

Microstructures were investigated using an Olympus BX51 optical microscope and a Zeiss Auriga field emission gun scanning electron microscope (FEG-SEM) with a BRUKER e-FlashHR electron backscatter diffraction (EBSD) detector by a combination of imaging and orientation mapping. The crystal facets, growth directions, and orientation relationships (ORs) between phases were determined from the EBSD data using Bruker Esprit 2.0 software.

Some $Ag_3Sn$ eutectic plates were thin enough for transmission electron microscopy (TEM) analysis. To prepare samples, $\beta$-Sn was selectively etched away, releasing $Ag_3Sn$ plates or rods that were rinsed with ethanol and transferred onto a TEM grid using a dropper. After ethanol evaporation, thin $Ag_3Sn$ plates/rods lay flat on the grid without need for further sample preparation. TEM imaging and selected area electron diffraction (SAED) were conducted using a Jeol 2100Plus.

For indexing of SEM-EBSD patterns and TEM-SAED patterns, the $Ag_3Sn$ and $\beta$-Sn crystal structures in Table I were assumed. Note that orthorhombic $Ag_3Sn$ has the $D0_a$ structure type[38–41] which is a chemically ordered derivative of the HCP structure.[42] The unit cell is described with different axis selections and slightly different orthorhombic

**Table I. Crystal Structures and Lattice Parameters Assumed for Indexing SEM-EBSD and TEM-SAED Patterns Data are Taken from Refs. [40], [43]**

| Phase | System | P.S | S.G | S.D | $a$ [Å] | $b$ [Å] | $c$ [Å] |
|---|---|---|---|---|---|---|---|
| $Ag_3Sn$ | orthorhombic | oP8 | Pmmn | $D0_a$ | 4.782 | 6.000 | 5.164 |
| $\beta$-Sn | tetragonal | tI4 | $I4_1/amd$ | A5 | 5.831 | — | 3.182 |

*P.S.* pearson symbol, *S.G.* space group, *S.D.* Strukturbericht designation.

distortions in References 38 through 40; here we use the unit cell of Rossi *et al.*[40]

## III. RESULTS AND DISCUSSION

### A. *Eutectic Morphologies and the Crystallography of Growth*

Figure 1 overviews the range of growth morphologies in binary Sn–Ag alloys after laboratory directional solidification. Figure 1(a) shows a transverse section of the plate-like fully eutectic microstructure in Sn–4Ag grown at $V = 2\ \mu m\ s^{-1}$, where the growth direction is out of the page. The plate-like eutectic grew with two morphologies and the micrograph in Figure 1(a) was chosen as it contains both of these morphologies, one in each of the two eutectic grains. In the left grain (Figure 1(a)), the $Ag_3Sn$ plates are well aligned in a 'broken lamellar' eutectic morphology. In the right grain, the $Ag_3Sn$ plates have a disordered alignment giving an irregular plate morphology.

Figure 1(b) shows a $\beta$-Sn dendrite plus $\beta$-Sn + $Ag_3Sn$ eutectic microstructure in a transverse section of Sn–4Ag at $V = 100\ \mu m\ s^{-1}$, where the nonfaceted $\beta$-Sn dendrite arms are surrounded by rod-like $\beta$-Sn + $Ag_3Sn$ eutectic.

Figure 1(c) shows a typical primary $Ag_3Sn$ crystal where the growth direction was from left to right. The growth morphology is a faceted plate with growth tips that have begun to branch. Primary $Ag_3Sn$ crystals were present in hypereutectic alloys Sn–4.5Ag and Sn–5.5Ag in the initial transient stages of growth and were always outcompeted by other growth fronts at steady state for the solidification conditions studied in this work.

Transverse sections of steady state growth for different growth velocities are shown in Figure 2. The growth direction is out of the page and the sections are about 3 mm behind the quenched interface. Figures 2(a) through (d) overview the lengthscale and morphology changes of eutectic $\beta$-Sn + $Ag_3Sn$ for different growth velocities. At $V = 2\ \mu m\ s^{-1}$, eutectic $\beta$-Sn + $Ag_3Sn$ contains relatively thick $Ag_3Sn$ plates and a wide eutectic spacing; the example in Figure 2(a) is from the broken-lamellar morphology. As the velocity increases, the thickness of eutectic $Ag_3Sn$ and the eutectic spacing decrease, and there is a transition from $Ag_3Sn$ plates to rods (Figures 2(c) through (d)). These morphological changes are consistent with past directional solidification studies on Sn–Ag alloys.[14–16,20]

For plates, the eutectic spacing was measured using the length of lines perpendicular to the plates (L) and the number of spacings (n) with $\lambda = L/n$. For rods, the spacing was measured using the number of rods per unit area (N/A) with $\lambda = 0.8(N/A)^{-0.5}$.[44] Figure 2(e) shows a plot of eutectic spacing against $1/\sqrt{V}$ for the range of growth velocity $V = 1$–$400\ \mu m\ s^{-1}$. Error bars are standard deviations of all measured values. At velocities higher than $2\ \mu m\ s^{-1}$ which corresponds to $V^{-0.5} < 0.7\ \mu m^{0.5}\ s^{-0.5}$ in Figure 2(e), the eutectic has a broken-lamellar or rod morphology and the measured eutectic spacings are in good agreement with a $\lambda \propto 1/\sqrt{V}$ relationship with a gradient of $9.01\ \mu m^{1.5}\ s^{-0.5}$ and $R^2 = 0.97$. At lower growth velocity, $V \leq 2\ \mu m\ s^{-1}$ which corresponds to $V^{-0.5} \geq 0.7\ \mu m^{0.5}\ s^{-0.5}$ in Figure 2(e), the eutectic has an irregular plate morphology (nonaligned plates in Figure 1(a)), and the measured eutectic spacings span a wider range and the mean spacings are much higher than the $\lambda = 9.01/\sqrt{V}$ linear relationship of the broken-lamellar and rod eutectic. A wider mean spacing in the highly irregular plate eutectic is consistent with past work which has shown that irregular eutectics have greater difficulty in adjusting their spacing which causes them to grow with a wider range of spacings and, on average, to grow further from the minimum spacing in the undercooling-spacing relationship.[45–49]

Literature data on the $\beta$-Sn + $Ag_3Sn$ eutectic velocity–spacing relationship are summarized in Table II.[13,15,16] Past work has reported a linear relationship between eutectic spacing and $1/\sqrt{V}$. However, the past studies show significant differences in the slope of the constant $= \lambda\sqrt{V}$. This seems to be partly because different studies report their $\lambda\sqrt{V} =$ constant value over different velocity ranges and therefore different morphology ranges, and because authors use different methods to measure the spacing in nf–f eutectics. When considering our data for the rod-like eutectic only ($V \geq 20\ \mu m\ s^{-1}$), our $\lambda\sqrt{V}$ = constant value is similar to Esaka *et al.*'s[15] value for growth at $V \geq 16.7\ \mu m\ s^{-1}$ and both studies used a similar method for calculating the rod spacing.

Table II also shows an effect of the temperature gradient. Combining all studies in Table II, the $\lambda\sqrt{V} =$ constant value decreases as the temperature gradient $G_L$ increases. This is consistent with previous work on nf–f eutectics including Al–Si[32] and Fe–C[50] and more recent research on Sn–Ag and Sn–Ag–Cu.[16,51] The role of the temperature gradient is usually explained in terms of the non-isothermal nature of a nf–f eutectic front: a steeper temperature gradient acts to flatten the front, rendering solute diffusion away from growth tips less effective which promotes constitutional supercooling and, therefore,

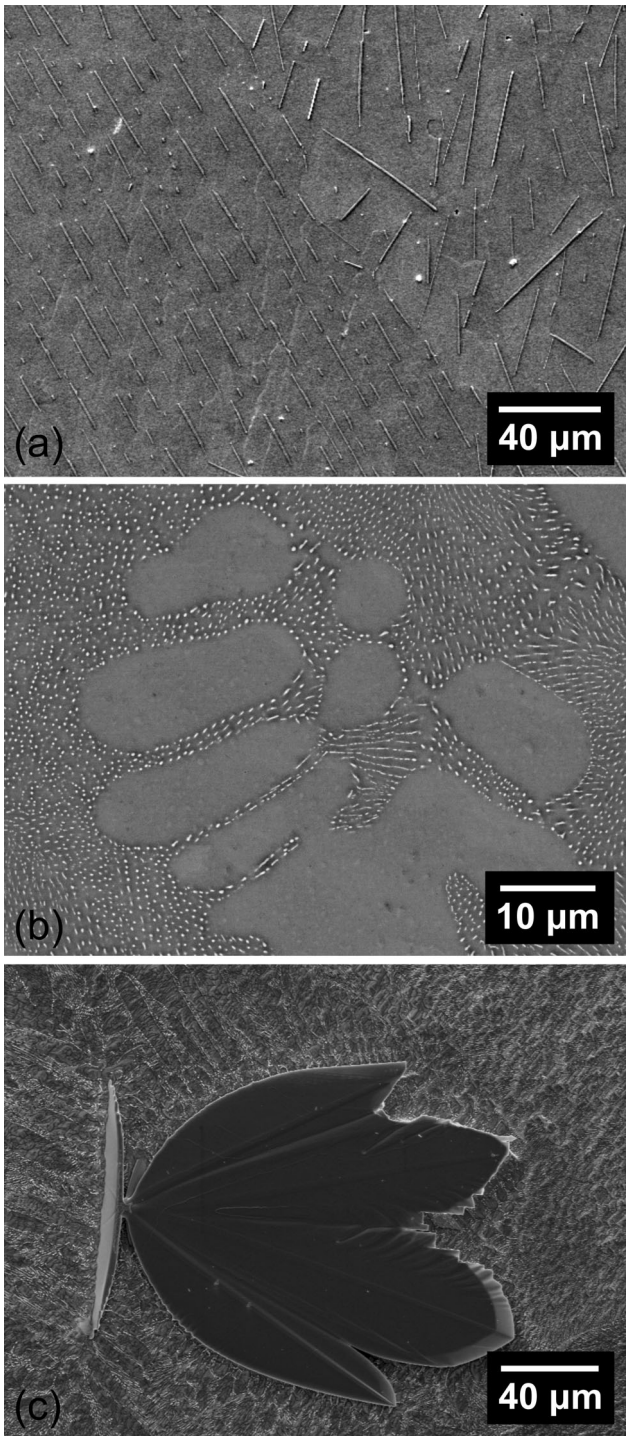


Fig. 1—Typical microstructures of binary Sn–Ag alloys after Bridgman growth at $G_L$ = 12 K/mm. (*a*) broken-lamellar and irregular plate eutectic in Sn–4Ag at $V$ = 2 $\mu$m s$^{-1}$; (*b*) $\beta$-Sn dendrites plus rod eutectic in Sn–4Ag at $V$ = 100 $\mu$m s$^{-1}$; (*c*) Primary $Ag_3Sn$ during initial transient growth in Sn–4.5Ag at $V$ = 500 $\mu$m s$^{-1}$. In (a) and (b), growth direction is out of the image. In (c), growth direction is from left to right.

branching which brings the mean spacing closer to the extremum spacing (*e.g.*, Reference 48).

The aspect ratio ($Ag_3Sn$ width against thickness in transverse sections) of eutectic $Ag_3Sn$ is plotted for growth velocities from $V$ = 2 $\mu$m s$^{-1}$ to $V$ = 400 $\mu$m s$^{-1}$ as square symbols in Figure 2(f). The aspect ratio is higher than 10 for growth velocities lower than 20 $\mu$m s$^{-1}$ corresponding to thin $Ag_3Sn$ plates. The aspect ratio decreases gradually from a growth velocity $\approx$ 20 $\mu$m s$^{-1}$ where the eutectic $Ag_3Sn$ is a mixture of plates and rods as in Figure 2(c). For growth velocity higher than 40 $\mu$m s$^{-1}$, the aspect ratio is only slightly higher than 1 and the $Ag_3Sn$ morphology is rod-like (Figure 2(d)). The aspect ratio measurements are compared with the work of Esaka *et al.*[15] in Figure 2(f). Both sets of results show a similar trend, and the aspect ratio decreases around a similar growth velocity. However, the aspect ratio for plates is three times higher for Esaka *et al.*[15] than our results. One factor behind this is the different compositions used: Sn–3.5Ag by Esaka *et al.*[15] and Sn–4Ag in our work. This will lead to a higher volume fraction of $Ag_3Sn$ in fully eutectic microstructures and consequently to thicker $Ag_3Sn$ plates for the same spacing, leading to a lower aspect ratio. Esaka *et al.* also used thicker samples (5 mm *vs.* 0.5 mm) and a longer growth distance (100 mm *vs.* 21 mm) which may have enabled plates to form a more stable array.

$\beta$-Sn + $Ag_3Sn$ is a nf–f eutectic that might be expected to grow as an irregular eutectic based on most eutectic classification systems.[52,53] However, while the $\beta$-Sn + $Ag_3Sn$ eutectic grew with irregular plate morphology at growth velocity lower than 3 $\mu$m s$^{-1}$, it grew with well-aligned broken lamellae at intermediate growth rates and aligned rods at higher growth velocity, indicating that crystallographic locking,[54–56] *i.e.,* growth with a fixed orientation relationship, may be important. The crystallography associated with each growth form is presented next.

The crystallography of eutectic $Ag_3Sn$ growth was found to be the same for all eutectic growth morphologies (irregular plate, broken-lamellar, and rod-like) based on SEM-EBSD and TEM-SAED analysis. A typical result is shown in Figure 3 using as an example a flattened $Ag_3Sn$ rod that was thin enough for TEM directly after deep etching. Figure 3(a) shows a bright-field TEM image where the largest facet normal is in the electron beam direction and the growth direction can be clearly seen. The SAED pattern in Figure 3(b) is from the beam direction parallel to [001] as can be confirmed from the calculated pattern in Figure 3(c). The rotational (azimuthal) positions of the diffraction spots in Figures 3(b) and (c) enabled lattice directions to be deduced as annotated on Figure 3(a). From this, the $Ag_3Sn$ growth direction is $< 010 >$ and the main growth facet is {001}. Note that $Ag_3Sn$ is orthorhombic so $\langle 100 \rangle \neq \langle 010 \rangle \neq \langle 001 \rangle$.

Table III summarizes the crystallographic aspects of eutectic $\beta$-Sn in four samples measured by EBSD. The number of $\beta$-Sn grains decreased with growth distance, and each sample only had one $\beta$-Sn grain across the cross-section in the late stage of steady state growth where the micrographs in Figure 1 and spacing measurements were taken. The orientation of this final eutectic $\beta$-Sn was $\langle 010 \rangle_{Sn}$ or $\langle 110 \rangle_{Sn}$ close to the pulling direction. For the irregular plate morphology at low growth rate, it was found that the $Ag_3Sn$ plates were

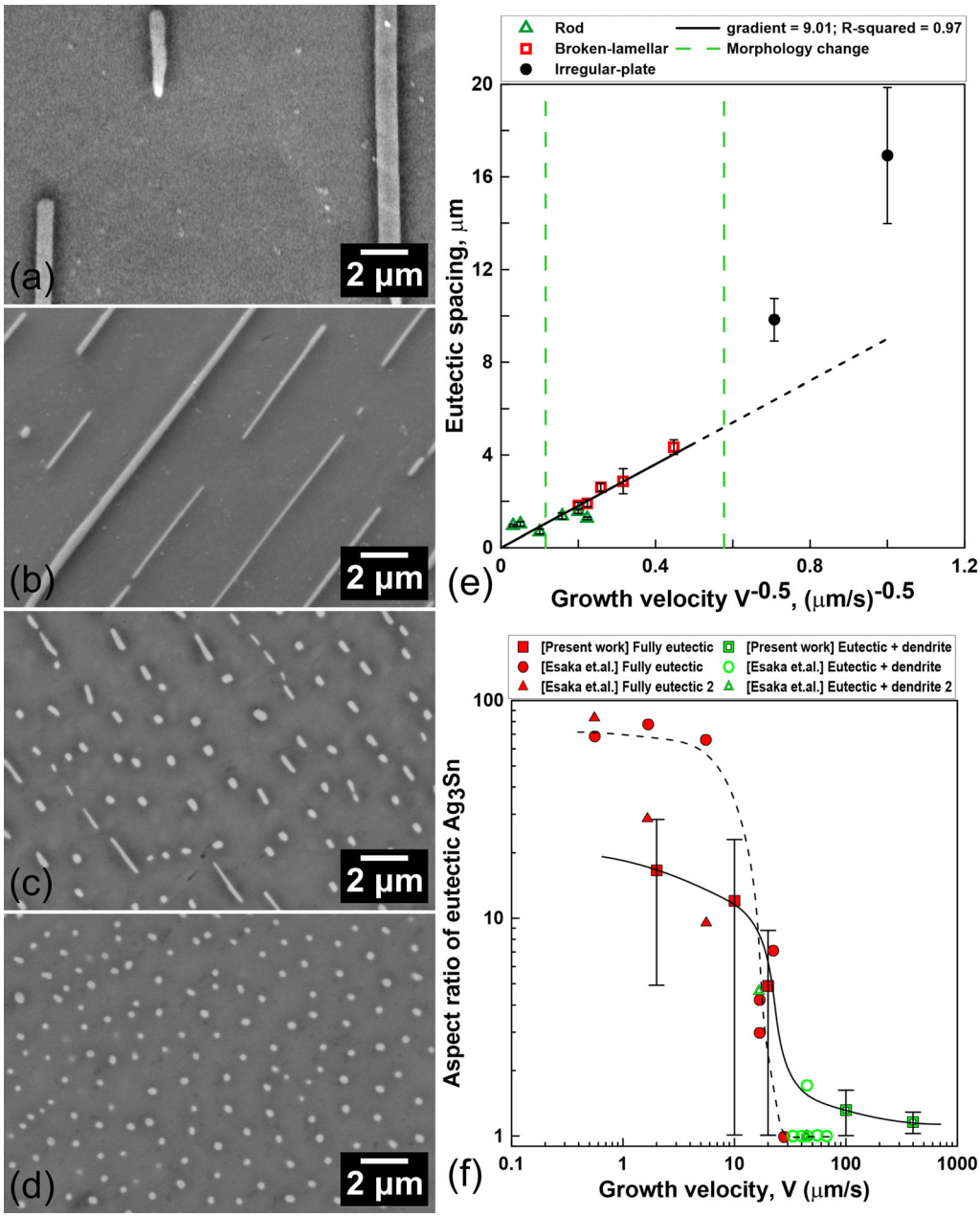


Fig. 2—Transverse sections of steady state growth of Sn–4Ag at $G_L$ = 12 K/mm for (*a*) $V$ = 2 $\mu$m s$^{-1}$; (*b*) $V$ = 10 $\mu$m s$^{-1}$; (*c*) $V$ = 20 $\mu$m s$^{-1}$; (*d*) $V$ = 400 $\mu$m s$^{-1}$. (*e*) Plot of eutectic spacing against to $1/\sqrt{V}$ in Sn–4Ag; (*f*) Plot of aspect ratio of eutectic $Ag_3Sn$ against growth velocity. Squares are present work. Circles and triangles are taken from [15]..

**Table II. Summary of Studies on the Eutectic Spacing–Velocity Relationship in Sn–Ag Alloys**

| Year | References | $C_0$ [wt pct Ag] | $G_L$ [K.mm$^{-1}$] | $\lambda\sqrt{V}$ [$\mu$m$^{1.5}$ s$^{-0.5}$] | V Range [$\mu$m s$^{-1}$] | Eutectic Morphology |
|---|---|---|---|---|---|---|
| 1968 | Moore and Elliott[13] | — | 0.05 | 13.68 | 0.7 to 14 | — |
| 2005 | Esaka[15] | 3.5 | 5.2 | 7.66 | 16.7 to 66.3 | rod |
| 2012 | Şahin and Çadirli[16] | 3.5 | 3.93 | 12.6 | 8.3 to 500 | rod |
| | this work | 4 | 12 | 8.97 | 5 to 400 | broken-lamellar to rod |
| | | 4 | 12 | 7.29 | 20 to 400 | rod |

oriented at a wide range of angles with respect to the surrounding $\beta$-Sn and, typically, no preferred or simple OR between the phases was present. An example of this is given in supplementary Figure S1, which is an EBSD map containing multiple $Ag_3Sn$ irregular plates within a single grain of $\beta$-Sn. The pole figures and unit cell wireframe orientations confirm that all $Ag_3Sn$ plates grew along their $\langle 010 \rangle$ direction, each $Ag_3Sn$ plate had a different orientation with respect to the $\beta$-Sn grain, and none had a reproducible or simple OR with the surrounding $\beta$-Sn orientation.

In contrast, when the eutectic grew with a broken-lamellar or rod morphology, two reproducible ORs were found in eutectic $\beta$-Sn + $Ag_3Sn$ and the same ORs were measured for both the broken-lamellar and rod-like morphology. Figure 4 shows EBSD mapping of regions with OR1 and OR2 using three examples in Sn–4Ag. Each example is a transverse section with growth out of the page. In the EBSD phase maps and plotted unit cells, blue is $\beta$-Sn and green is $Ag_3Sn$. Figures 4(a) through (f) show broken-lamellar $\beta$-Sn + $Ag_3Sn$ eutectic grown at $V = 10\ \mu m\ s^{-1}$ and Figures 4(g) through (l) show a region of rod-like $\beta$-Sn + $Ag_3Sn$ eutectic grown at $V = 20\ \mu m\ s^{-1}$, both with OR1. In both Figures 4(a) through (f) and Figures 4(g) through (l), the pole figures for selected planes in $Ag_3Sn$ and $\beta$-Sn show the following near-parallel planes: $(100)_{Ag_3Sn}//(101)_{Sn}$, $(010)_{Ag_3Sn}//(010)_{Sn}$, and $(001)_{Ag_3Sn}//(301)_{Sn}$. The growth direction is $[010]_{Ag_3Sn}//[010]_{Sn}$ and the plate main facet is $(001)_{Ag_3Sn}$. OR1 can be written as

$$(001)_{Ag_3Sn}//(301)_{Sn} \text{and } [010]_{Ag_3Sn//}[010]_{Sn}\ \text{OR1}$$

Figures 4(m) through (r) show an example of OR2 in Sn–4Ag grown at $V = 400\ \mu m\ s^{-1}$. The unit cell wireframes and pole figures show the following parallel planes: $(100)_{Ag_3Sn}//(100)_{Sn}$, $(010)_{Ag_3Sn}//(010)_{Sn}$, and $(001)_{Ag_3Sn}//(001)_{Sn}$. The common growth direction, [010]$Ag_3Sn$//[010]Sn, is the same in OR1 and OR2. Thus, OR2 can be written as

$$(001)_{Ag_3Sn}//(001)_{Sn} \text{and } [010]_{Ag_3Sn}//[010]_{Sn}\ \text{OR2}$$

It can also be seen in Figures 4(m) through (r) that the rods do not have a circular section but are flattened, and the largest facet of the rod is the (001) plane, consistent with the TEM analysis in Figure 3 and the same as the main facet of $Ag_3Sn$ plates in Figures 4(a) through (f). Similar flattened rods were very common and are likely to result from the anisotropy in the $\beta$-Sn + $Ag_3Sn$ interfacial energy (*i.e.*, the lower energy interface is the flattened (larger) $\beta$-Sn + $Ag_3Sn$ interface).

The two ORs are the same as those reported by Ma *et al.*[57] for the nucleation of $\beta$-Sn droplets on relatively large $Ag_3Sn$ single crystals. That work[57] showed that the two ORs are related to each other *via* a twin relationship in $\beta$-Sn, and that there is a similar lattice match for both ORs. Table IV summarizes the frequency of measurement of the two ORs and their measured misorientation angles. The ratio of occurrence of OR1:OR2 was 13:5, indicating that OR1 may have the lower interfacial energy. The atomic matching analysis in the interfacial plane for OR1 and OR2 in[57] shows that OR1 does indeed have the slightly smaller (better) atomic disregistry.

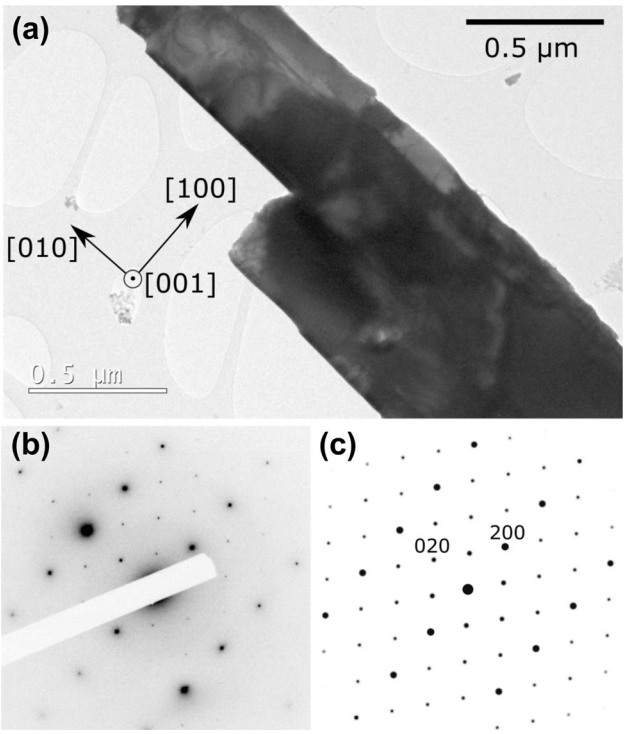


Fig. 3—TEM analysis of $Ag_3Sn$ growth crystallography. (*a*) Brightfield TEM image of a eutectic $Ag_3Sn$ flat rod. (*b*) Experimental SAED pattern from the plate in (a). (*c*) calculated SAED pattern along [001] zone axis with indexing, confirming the plate orientation annotated on (a).

**Table III. Number of Sn Grains Through the Whole Sample in Longitudinal Section**

| Sample | V ($\mu m\ s^{-1}$) | Growth Distance (mm) | | | | | | | | | | | | Pulling Direction |
|---|---|---|---|---|---|---|---|---|---|---|---|---|---|---|
| | | 0 | 2 | 4 | 6 | 8 | 10 | 12 | 14 | 16 | 18 | 20 | 22 | |
| 1 | 0.5 | 4 | 4 | 2 | 3 | 2 | 2 | 2 | 2 | 2 | 2 | 2 | 1 | [010]Sn |
| 2 | 0.5 | 6 | 5 | 4 | 3 | 3 | 2 | 1 | 1 | 1 | 1 | 1 | 1 | [010]Sn |
| 3 | 1 | 6 | 4 | 2 | 1 | 1 | 1 | 1 | 1 | 1 | 1 | 1 | 1 | [010]Sn |
| 4 | 2 | 7 | 3 | 3 | 2 | 3 | 2 | 2 | 1 | 1 | 1 | 1 | 1 | [110]Sn |

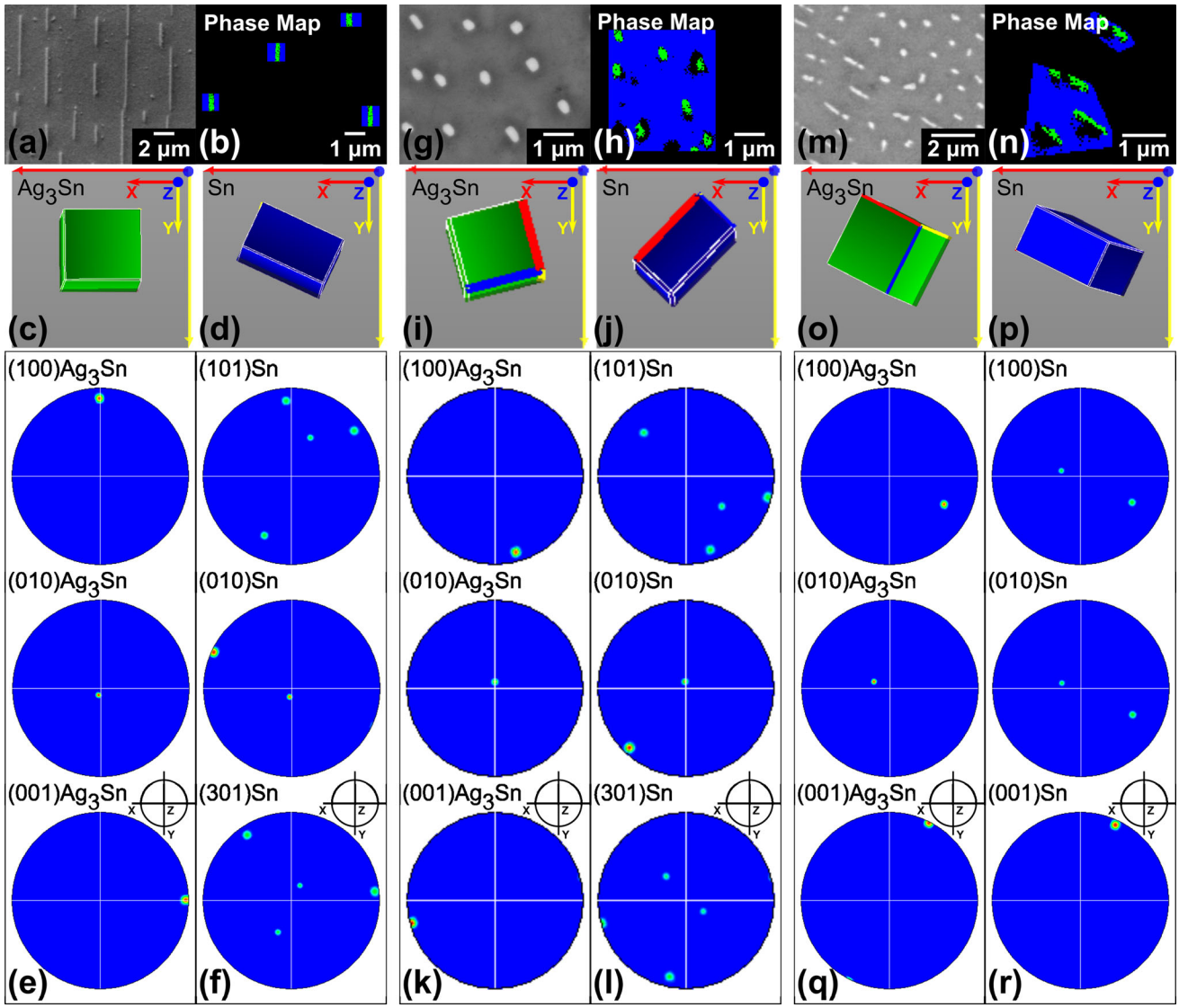


Fig. 4—EBSD analysis of orientation relationships (ORs) in regular regions of $\beta$-Sn + $Ag_3Sn$ eutectic in Sn–4Ag grown at $G_L$ = 12 K/mm. Growth is into the page. In phase maps, blue is $\beta$-Sn and green is $Ag_3Sn$. (*a*) through (*f*) OR1 at $V$ = 10 $\mu$m $s^{-1}$; (*g*) through (*l*) OR1 at $V$ = 20 $\mu$m $s^{-1}$; (*m*) through (*r*) OR2 at $V$ = 400 $\mu$m $s^{-1}$ (Color figure online).

**Table IV. Summary of Two ORs and Their Average Misorientation Angles (MOAs)**

| | Growth Direction | OR1 | | OR2 | |
|---|---|---|---|---|---|
| | [010]$Ag_3Sn$// [010]Sn | (001)$Ag_3Sn$ // (301)Sn | (100)$Ag_3Sn$ // (101)Sn | (001)$Ag_3Sn$ // (001)Sn | (100)$Ag_3Sn$ // (100)Sn |
| MOA (Degree) | 3.58 ± 3.14 | 5.82 ± 2.52 | 4.35 ± 1.84 | 3.35 ± 2.22 | 5.60 ± 3.29 |
| Frequency | 18/18 | 13/18 | | 5/18 | |

Table V summarizes the frequency of occurrence of the ORs at different growth velocities. The ORs were rarely found when the morphology was irregular plates (at $V \leq 2$ $\mu$m $s^{-1}$). In contrast, the ORs formed in 100 pct of samples during broken-lamellar and mixed broken-lamellar + rod growth at 3 to 20 $\mu$m $s^{-1}$. At higher velocity, less than 50 pct of measured samples had the eutectic ORs. These velocities ($\geq$ 100 $\mu$m $s^{-1}$) correspond to rod eutectic growth where $\beta$-Sn dendrites were present for $C_0$ = Sn–4.0 wt pct Ag. From these results, it can be seen that the transition from the irregular plate to broken-lamellar morphology is a transition to a crystallographically locked eutectic, and at higher velocity, the presence of $\beta$-Sn dendrites prevents the eutectic from maintaining full crystallographic locking during growth. The competition

Table V. Frequency of Eutectic Orientation Relationships (OR1 and OR2) at Different Growth Velocities in Sn–4Ag

| Eutectic Morphology | Irregular Plate | | | Broken- lamellar | | Mixed | | Rod | |
|---|---|---|---|---|---|---|---|---|---|
| Growth Velocity ($\mu$m s$^{-1}$) | 0.5 | 1 | 2 | 3 | 10 | 20 | 100 | 400 | 1000 |
| ORs Frequency | 0/6 | 0/1 | 2/5 | 2/2 | 6/6 | 4/4 | 2/5 | 2/4 | 1/4 |

between $\beta$-Sn dendrites and a eutectic front is considered in Section III–C. Both the broken-lamellar and rod morphologies had $< 010 >$ $Ag_3Sn$ crystallographic growth orientation, {001} as the largest interface and OR1 or OR2 with $\beta$-Sn. Therefore, in this system, the transition from broken-lamellar to rod eutectic growth is not related to a change in crystallographic orientation.

## B. *Mechanisms of Spacing and Morphology Adjustment*

### 1. *Rod ↔ broken-lamellar transitions*

Figure 5 overviews the mechanisms by which the eutectic undergoes a transition from broken-lamellar to rod morphology and vice versa after a velocity change to/from 5 and 20 $\mu$m s$^{-1}$. Figure 5(i) and (ii) give the typical steady state morphologies in transverse cross-sections: broken-lamellar at 5 $\mu$m s$^{-1}$ and rod at $V = 20$ $\mu$m s$^{-1}$. The morphology changes when a sample growing at $V = 5$ $\mu$m s$^{-1}$ was increased to $V = 20$ $\mu$m s$^{-1}$ are shown in Figures 5(A) through (F). These images were taken after etching to selectively remove the $\beta$-Sn to better reveal the faceted $Ag_3Sn$ morphology. The $Ag_3Sn$ has a plate microstructure initially at $V = 5$ $\mu$m s$^{-1}$ with serrated edges on the sides of the plates. In the transient region after the velocity increase, the width of $Ag_3Sn$ plates reduces by some regions of the edges stopping growing and some protrusions on the serrated edges growing out as branches (Figure 5(E)). This branching ultimately develops into an array of rods at $V = 20$ $\mu$m s$^{-1}$. Figure 5(F) shows that the rods are flattened where the flattened surface is the same facet plane as the largest surface of the original plates. This is consistent with the measurement of a (001) facet on both plates and flattened rods in the previous section.

A sample that was growing at $V = 20$ $\mu$m s$^{-1}$ and then decreased to $V = 5$ $\mu$m s$^{-1}$ is shown in Figures 5(a) through (f). The $\beta$-Sn + $Ag_3Sn$ eutectic initially grows with a parallel rod array at $V = 20$ $\mu$m s$^{-1}$. Once the growth velocity decreases to $V = 5$ $\mu$m s$^{-1}$, many rods branch into a 'Y' shape (Figure 5(e)) and, with further growth, the 'Y' shapes fill in to form plates (*e.g.*, Figure 5(c)) that develop into aligned plates (Figure 5(f)).

### 2. *Synchrotron radiography*

Figure 6 shows $\beta$-Sn + $Ag_3Sn$ eutectic growth at $G_L = 6.5$ K/mm under vertical (upward) directional growth. Figures 6(a) and (c) show radiography images of $\beta$-Sn + $Ag_3Sn$ eutectic growth at $V = 1$ $\mu$m s$^{-1}$ and $V = 10$ $\mu$m s$^{-1}$, respectively. The top of the images is liquid, and the bottom is $\beta$-Sn + $Ag_3Sn$ eutectic. At $V = 1$ $\mu$m s$^{-1}$, $Ag_3Sn$ grows with triangular faceted tips protruding in front of the $\beta$-Sn + L interface and $Ag_3Sn$ forms a plate morphology with overlapping sheets in the through-thickness averaged radiographs of Figure 6(a), where the large surface of $Ag_3Sn$ is parallel to the page. Figure 6(b) shows a 'post-mortem' SEM image from the same synchrotron sample as Figure 6(a) at $V = 1$ $\mu$m s$^{-1}$, showing this plate morphology.

Figure 6(c) shows the growth front at the higher velocity of $V = 10$ $\mu$m s$^{-1}$. The $Ag_3Sn$ are small near-vertical lines in the radiography image, and they have a well-aligned plate morphology where the large surface of $Ag_3Sn$ intersects the page as shown in the 'post-mortem' SEM images in Figures 6(d) and (e). Comparing Figures 6(a) and (c) provides insights into the solid/liquid interfaces at the nf–f eutectic growth front. In Figure 6(a), the eutectic growth front is non-isothermal with the faceted $Ag_3Sn$ phase leading the $\beta$-Sn phase as is common in nf–f eutectics. In Figure 6(c), the non-isothermal front becomes narrower as the interface velocity increased but the $Ag_3Sn$ still protrudes ahead.

Figure 7 shows sequences of radiography images involving changes in the eutectic front during velocity changes in Sn–3.7Ag at $G_L = 6.5$ K/mm to/from $V = 1$–10 $\mu$m s$^{-1}$. The growth direction is from the bottom upward and the thermal gradient is hotter upward. Figures 7(A) through (D) show the morphology changes at increasing growth velocity from 1 to 10 $\mu$m s$^{-1}$. The $\beta$-Sn + L interface position is moving downwards in the images due to eutectic growth occurring at lower temperature at higher growth velocity. At $V = 1$ $\mu$m s$^{-1}$ in Figure 7(A), the eutectic morphology is irregular plates and $Ag_3Sn$ plates are both parallel to and intersect the page. The $\beta$-Sn + L interface is irregular with faceted $Ag_3Sn$ plates growing with a variety of local spacings and protruding slightly ahead of the front. As the growth velocity increases in Figure 7(B), the interface becomes flatter in most regions, but one region develops a large depressed $\beta$-Sn + L depth. This area has a large local eutectic spacing due to diverging plate growth and a larger local solute undercooling therefore develops. In the next seconds, some $Ag_3Sn$ plates branch and grow into the liquid in the depressed region where they reduce the local spacing as shown in Figure 7(C). This causes the depressed $\beta$-Sn + L interface to accelerate forwards, producing a flatter interface. With continued growth, the eutectic front becomes much flatter and smoother with better aligned plates (Figure 7(D)).

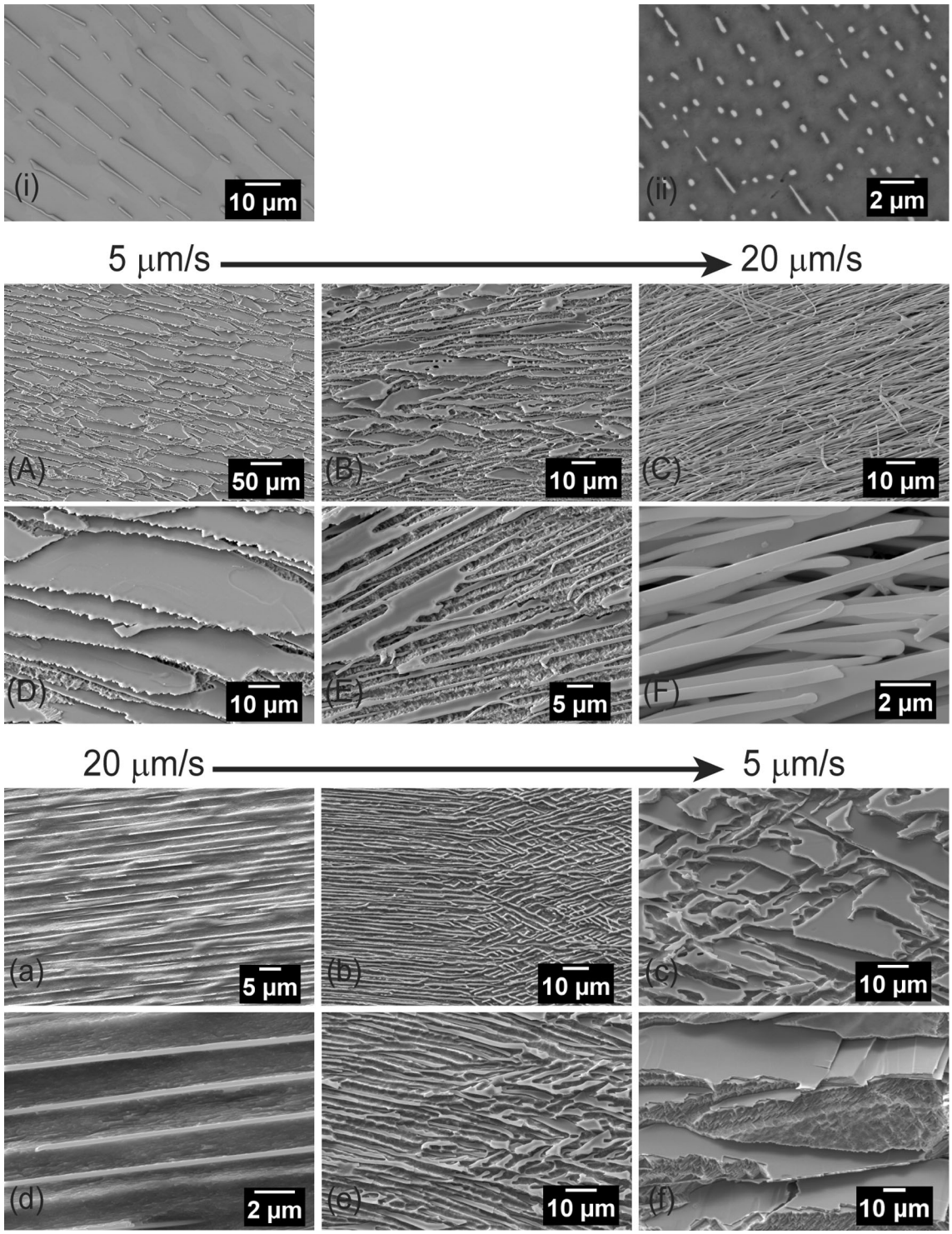


Fig. 5—Eutectic morphology development after growth velocity changes. (*A*) through (*F*): velocity increase from 5 to 20 $\mu$m s$^{-1}$. (*a*) through (*f*): velocity decrease from 20 to 5 $\mu$m s$^{-1}$. (*i*) and (*ii*): transverse sections after steady state growth at (i) $V = 3$ $\mu$m s$^{-1}$ and (ii) 20 $\mu$m s$^{-1}$. The $\beta$-Sn phase has been selectively etched in (A) through (F) and (a) through (f).

Figures 7(a) through (d) show morphology changes when decreasing growth velocity from 10 to 1 $\mu$m s$^{-1}$. The interface position is moving upward due to a hotter eutectic growth temperature at lower growth velocity. At $V = 10$ $\mu$m s$^{-1}$, the eutectic front is near-isothermal, and the morphology is well-aligned plate in Figure 7(a). As the growth velocity decreases, some $Ag_3Sn$ stop growing to increase the eutectic spacing in Figure 7(c). At 1 $\mu$m s$^{-1}$, the interface has some $Ag_3Sn$ plates growing ahead of the $\beta$-Sn + L interface with a protruding faceted tip (Figure 7(d)). The changing interface temperature is shown in

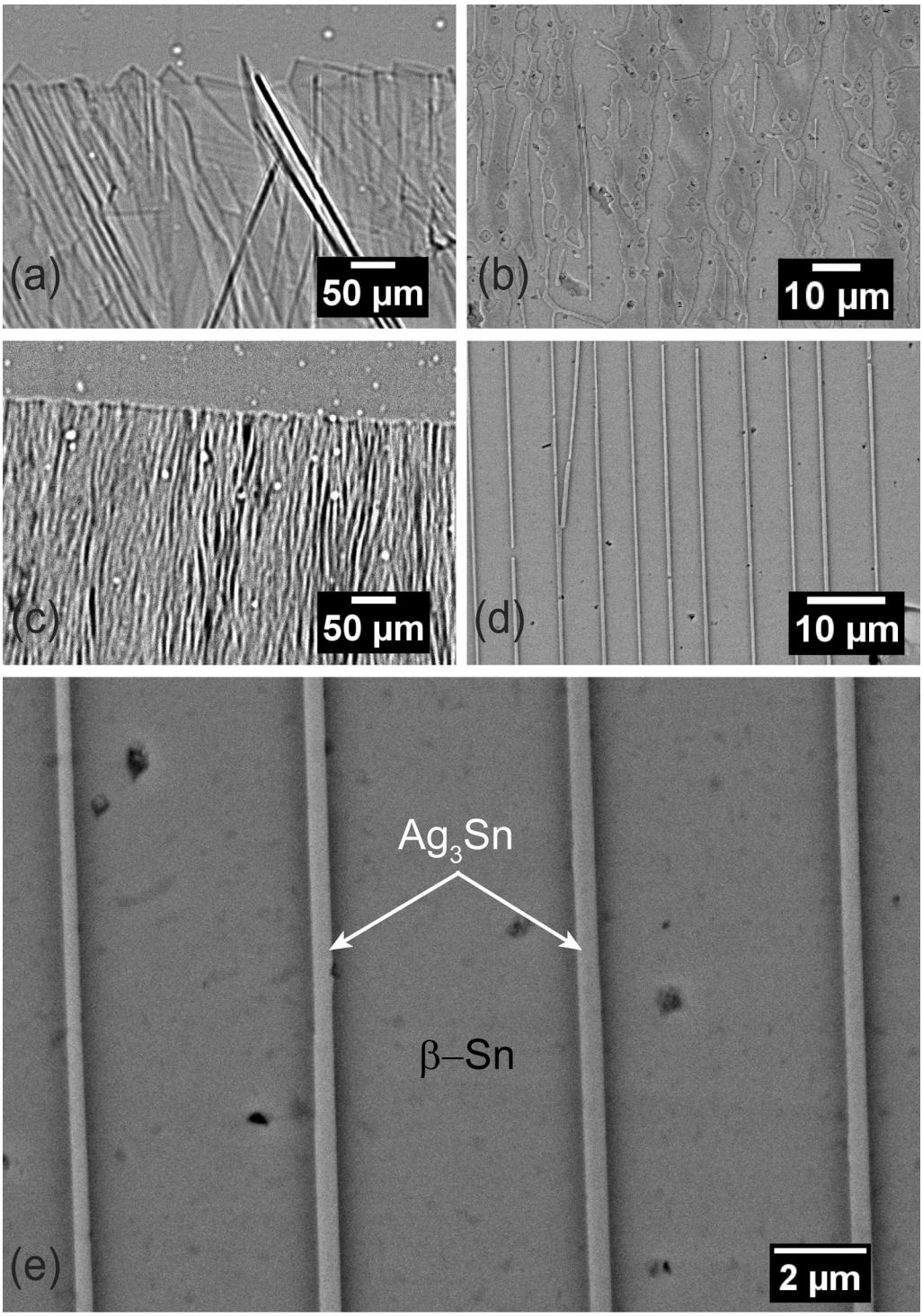


Fig. 6—$\beta$-Sn + $Ag_3Sn$ eutectic growth morphologies in thin-sample X-ray imaging experiments at $G_L$ = 6.5 K/mm in the vertical Bridgman rig. (*a*) X-ray image at $V$ = 1 $\mu$m $s^{-1}$. (*b*) post-mortem SEM image from the same sample as (a) at $V$ = 1 $\mu$m $s^{-1}$; (*c*) X-ray image at $V$ = 10 $\mu$m $s^{-1}$; (*d*) post-mortem SEM image from the same sample as (b) at $V$ = 10 $\mu$m $s^{-1}$; (*e*) higher magnification SEM image of (d).

Figure 8 as a plot of the mean interface position *vs* time during the velocity change experiment. The interface moves to hotter (colder) temperature as the velocity is decreased (increased) as expected of a $\Delta T = K\sqrt{V}$ eutectic growth undercooling relationship in nf–f eutectics.[13,31,32,45] However, this *in situ* experiment is not suitable for determining the constant of proportionality, $K$, as the eutectic front does not reach a steady vertical position at any of the growth rates applied.

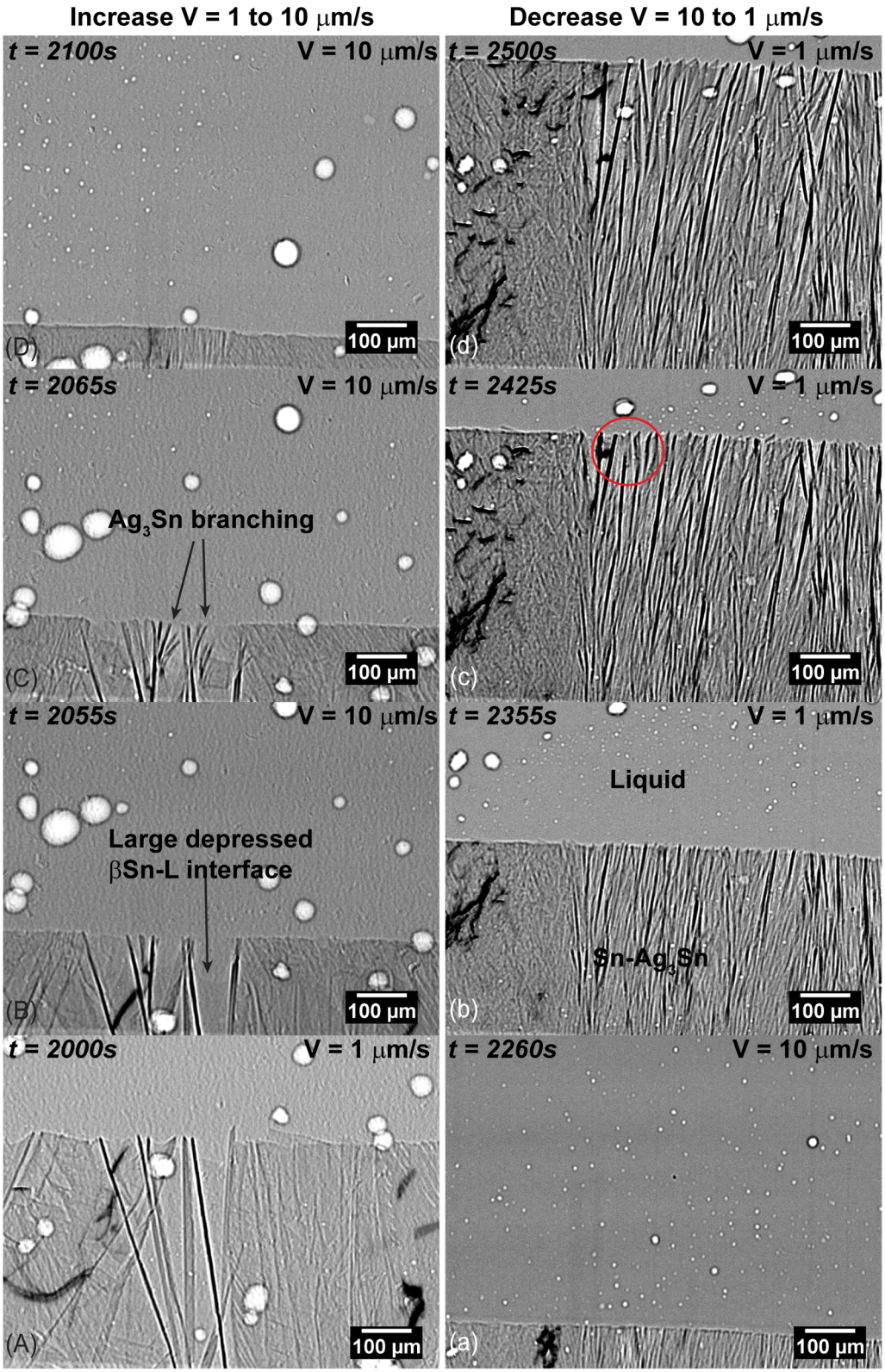


Fig. 7—Sequence of X-ray images of a eutectic front in Sn–3.7Ag at $G_L$ = 6.5 K/mm after velocity changes. (*A*) through (*D*) response to an increase from 1 to 10 $\mu$m s$^{-1}$; (*a*) through (*d*) response to a decrease from 10 to 1 $\mu$m s$^{-1}$.

Further insights can be gained from examination of the $Ag_3Sn$ leading distance in the eutectic. The local leading distance between $Ag_3Sn$ tips and the $\beta$-Sn + L interface was initially 30 ± 13 $\mu$m at $V$ = 1 $\mu$m s$^{-1}$ and then 4 ± 1 $\mu$m at $V$ = 10 $\mu$m s$^{-1}$, showing a decreasing $Ag_3Sn$ leading distance with increasing growth rate.

After a reduction in velocity from 10 $\mu$m s$^{-1}$ back to $V$ = 1 $\mu$m s$^{-1}$, the distance is 13 ± 5 $\mu$m which is significantly smaller than at 1 $\mu$m s$^{-1}$ before the increase to 10 $\mu$m s$^{-1}$. The microstructure at 1 $\mu$m s$^{-1}$ is more regular after a reduction from 10 $\mu$m s$^{-1}$ than before the increase to 10 $\mu$m s$^{-1}$. This seems to be related to the process by which the plates increase the local spacing on a velocity decrease: $Ag_3Sn$ plates that are poorly oriented for growth stop growing leaving the better oriented $Ag_3Sn$ plates in a more regular array. From the previous section, optimally oriented $Ag_3Sn$ plates have < 010 > in the growth direction and their (001) parallel with either $(001)_{Sn}$ or $(301)_{Sn}$, indicating that, on a decrease in velocity, plates close to these orientations will remain and those far from this orientation will stop growing to increase the spacing.

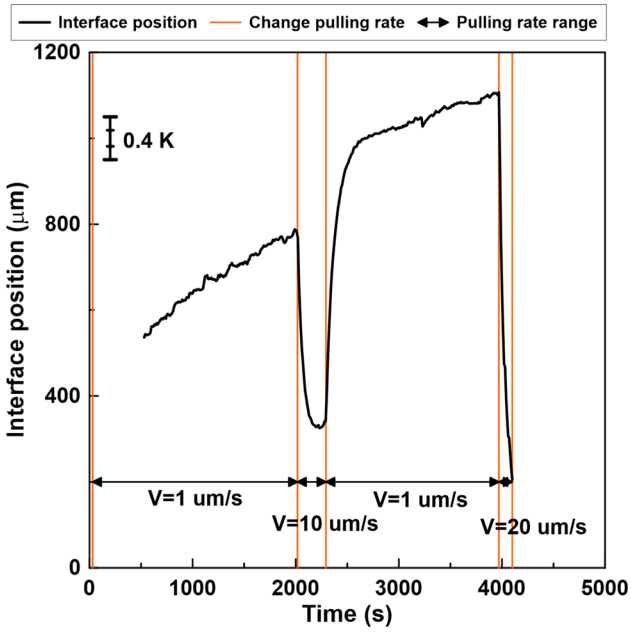


Fig. 8—Eutectic interface position against to time in X-ray Bridgman experiment. Sn–4Ag growth at $G_L$ = 6.5 K/mm. Radiographs taken in the range of $t$ = 2000s to $t$ = 2500 s are shown in Fig. 7.

## C. *Eutectic Coupled Zone*

Figure 9 shows the transition from fully eutectic growth to the growth of $\beta$-Sn dendrites plus eutectic in

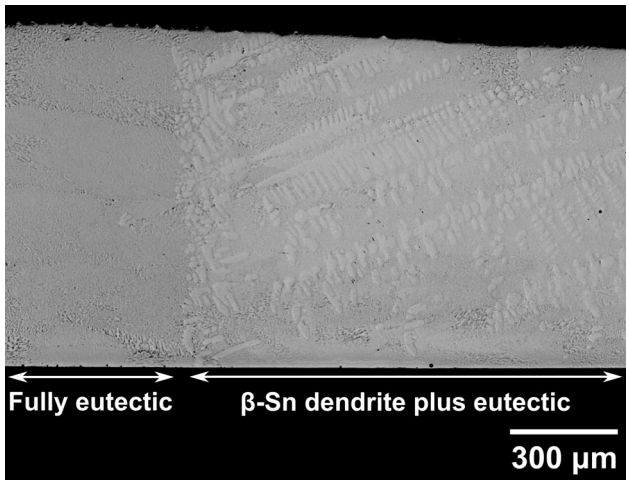


Fig. 9—Transition from fully eutectic microstructure to $\beta$-Sn dendrite-plus-eutectic in Sn–4Ag at $G_L$ = 12 K/mm and $V$ = 100 $\mu$m s$^{-1}$. Growth direction is from left to right.

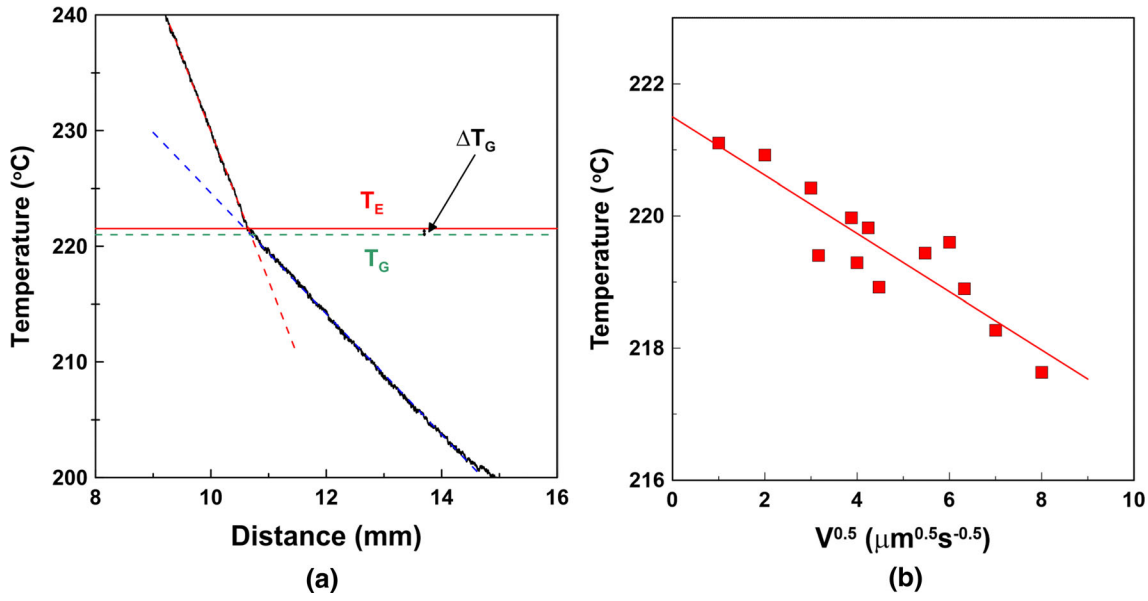


Fig. 10—(*a*) plot of eutectic growth temperature against to moving distance with a sketch of the method used to determine the eutectic growth temperature; (*b*) plot of eutectic growth temperature against $\sqrt{V}$.

Sn–4Ag grown at 100 $\mu$m s$^{-1}$. Note that the total growth distance in samples was 21 mm and the transition from eutectic to dendrites plus eutectic in samples occurred at a growth distance of less than 2 mm. We next investigate this type of transition by considering the growth temperatures of the eutectic front and dendrite tips.

Figure 10(a) shows a plot of the recorded temperature of an embedded thermocouple against the displacement of a Sn–4Ag sample at $V = 2$ $\mu$m s$^{-1}$, during which fully eutectic growth occurred. The plot contains a clear change in slope associated with the different thermal conductivities of the solid and liquid. The point where the gradient changes was defined as the eutectic growth temperature due to the eutectic front passing through. By this method, the eutectic growth temperatures for different growth velocities were measured, and the results are shown in Figure 10(b). Eutectic growth temperature is plotted *vs* $\sqrt{V}$ in expectation of this relationship in many nf–f eutectics[49,50] as well as in nf–nf eutectics.[58] The trend line is in reasonable agreement with the $\Delta T \propto \sqrt{V}$ relationship and the best fit gradient is ~ 0.44 Ks$^{0.5}$ $\mu$m$^{-0.5}$.

Sn–4Ag, Sn–4.5Ag, and Sn–5.5Ag grown under laboratory unidirectional solidification were used to determine the transition between fully eutectic and $\beta$-Sn dendrite-plus-eutectic microstructures. The results are shown in Figure 11(a) combined with data taken from the literature.[14,20,59] Solid red squares are fully eutectic microstructures and solid green squares are $\beta$-Sn dendrite-plus-eutectic microstructures from the present work. When combined with the literature data, the new datapoints confirm that the coupled zone is skewed to hypereutectic compositions (*i.e.,* the faceted $Ag_3Sn$ side). The transition velocities between fully eutectic and $\beta$-Sn dendrites plus eutectic are about 80 $\mu$m s$^{-1}$ for Sn–4Ag, 150 $\mu$m s$^{-1}$ for Sn–4.5Ag, and 150 $\mu$m s$^{-1}$ for Sn–5.5Ag. This shows that $\beta$-Sn dendrite tips can outcompete a $\beta$-Sn + $Ag_3Sn$ eutectic front and primary $Ag_3Sn$ at high velocity, even in these hypereutectic compositions.

In addition to the eutectic to dendrite-plus-eutectic transition shown in Figure 11, note that the other transitions in Sn–4Ag were irregular plate eutectic at $V < 2$ $\mu$m s$^{-1}$, broken-lamellar between 2 $\mu$m s$^{-1}$ < $V < 20$ $\mu$m s$^{-1}$, rod eutectic at $V > 40$ $\mu$m s$^{-1}$, and $\beta$-Sn dendrites plus rod eutectic above 80 $\mu$m s$^{-1}$. Note that, in all samples used for Figure 11, transverse sections were cut at 3 mm behind the quenched interface at a growth distance of ~ 18 mm, where a steady state microstructure was growing.

The measured undercooling–velocity relationship of the eutectic (Figure 10) was combined with analytical undercooling–velocity relationships for $\beta$-Sn dendrites taken from the literature[61–63] to explore the transition. Equation 1 describes the dendrite growth undercooling assuming growth is controlled by solute diffusion only around a hemispherical cap and approximating $I(P_c) = P_c\exp(P_c)E_1(P_c)$ by Ivantsov[64] as $I(P_c) \approx P_c$.[61,62]

$$\Delta T^{Sn1} = \pi\left(\frac{\Gamma m(k-1)}{D_L}\right)^{0.5} V^{0.5} C_0^{0.5} \qquad [1]$$

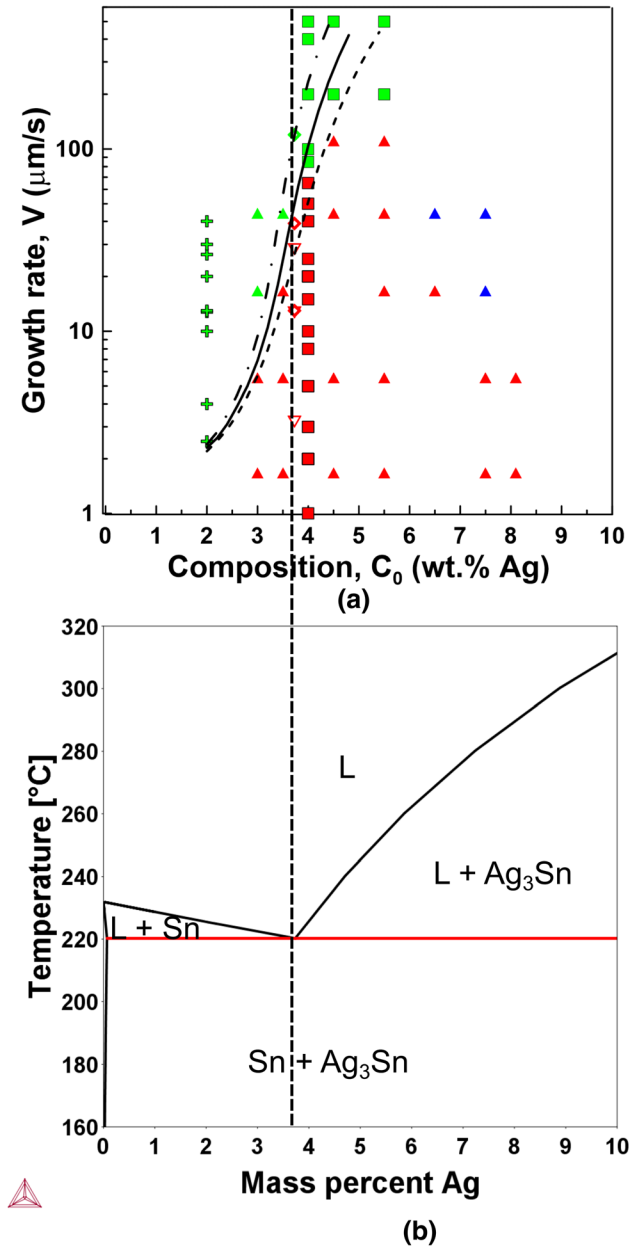


Fig. 11—(*a*) $C_0$-$V$ microstructure selection map for Sn–Ag. Red = eutectic microstructure. Green = $\beta$-Sn dendrite-plus-eutectic microstructure. Blue = primary $Ag_3Sn$ plus eutectic microstructure.∇ = Southin *et al.* [59]◇= Bromley *et al.* [14] Δ= Esaka *et al.* [20] ✚ = Yoshimura *et al.* [60] □ = present work. Calculated transition lines between fully eutectic and $\beta$-Sn dendrite-plus-eutectic: Dashed line with Eq. [1]; solid line with Eq. [2] dash-dot line with Eq. [3] (b) Binary Sn–Ag phase diagram (Color figure online).

Equation 2 describes the dendrite growth undercooling for the diffusion field around a 3D paraboloid of revolution and $I(P_c) \approx 1.5P_c^{0.8}$.[63]

$$\Delta T^{Sn2} = \left(\frac{5.51\pi\Gamma}{D_L}\right)^{0.4} (m(k-1))^{0.6} V^{0.4} C_0^{0.6} \qquad [2]$$

Table VI. Material Property Parameters of Sn–Ag System Used in the Transition Line Calculation

| Property | Symbol | Unit | Sn–$Ag_3Sn$ |
|---|---|---|---|
| Eutectic Temperature[a] | $T_E$ | °C | 221.5 |
| Eutectic Composition[b] | $C_E$ | wt pct | 3.73 |
| $\beta$-Sn Liquidus Slope[b] | $m_L^{\beta-Sn}$ | K/wt pct | -3.15 |
| IMC Liquidus Slope[b] | $m_L^{IMC}$ | K/wt pct | 20.12 |
| Mass Fraction $\beta$-Sn[b] | $f_{\beta-Sn}$ | pct | 94.98 |
| Mass Fraction IMC[b] | $f_{IMC}$ | pct | 5.02 |
| Density of $\beta$-Sn[b] | $\beta$-Sn | $Kg/m^3$ | 7290 |
| Density of IMC[b] | IMC | $Kg/m^3$ | 9920 |
| Volume Fraction $\beta$-Sn[b] | $g_{\beta-Sn}$ | pct | 96.26 |
| Volume Fraction IMC[b] | $g_{IMC}$ | pct | 3.74 |
| Solubility of $\beta$-Sn[b] | $C_{\beta-Sn}$ | wt pct | 0.06 |
| Solubility of IMC[b] | $C_{IMC}$ | wt pct | 73.15 |
| Partition Coefficient[b] | $K_0$ | — | 0.02 |
| Latent Heat of Fusion[c] | $L$ | J/kg | 59,212.54 |
| Specific Heat[c] | $c_p$ | J/Kg K | 223 |
| Thermal Diffusivity[c] | $\alpha_L$ | $m^2/s$ | $4.17 \times 10^{-5}$ |
| Solute Diffusivity[c] | $D_L$ | $m^2/s$ | $0.86 \times 10^{-9}$ |
| Gibbs-Thompson Coefficient of $\beta$-Sn[c] | $\Gamma_L^{\beta-Sn}$ | m.K | $7.85 \times 10^{-8}$ |
| Gibbs-Thompson Coefficient of IMC[c] | $\Gamma_L^{IMC}$ | m.K | $10.2 \times 10^{-8}$ |
| Angle Between $\beta$-Sn + L Interface and Vertical Line[a] | $\theta_{\beta-Sn}$ | deg | 10 |
| Angle Between IMC-L Interface and Vertical Line[a] | $\theta_{IMC}$ | deg | 20 |

[a]Measured data in present work.[b]Calculated by binary phase diagram in Fig. 11(b).[c]Taken from Refs. [47], [70] through [72].

Equation 3 is a fit to the dendrite growth undercooling from the Lipton–Glicksman–Kurz (LGK) model[65,66] accounting for solute diffusion and curvature, where the diffusion field is around a 3D paraboloid of revolution and $I(P_c) = P_c\exp(P_c)E_1(P_c)$.

$$\Delta T^{Sn3} = 0.27 C_0^{0.65} V^{0.35} \quad [3]$$

The terms in Eqs. [1–3] are defined in Table VI. For low growth velocity into a positive temperature gradient, GD/V was used to determine the growth undercooling and the two terms were combined to give the $\beta$-Sn tip temperature as a function of velocity in Eq. [4] as in References 31, 67–69:

$$T_G^{Sn} = T_{liq} - \left(\frac{GD}{V} + \Delta T^{Sn}\right) \quad [4]$$

The equivalent relationship for the eutectic growth temperature $T_G^E$ came from the measurements in Figure 10(b):

$$T_G^E = 221.5 - 0.44\sqrt{V} \quad [5]$$

To calculate the transition from fully eutectic to $\beta$-Sn dendrites plus eutectic growth, we used the properties in Table VI and the microstructure selection criterion that whichever microstructure can grow at highest temperature is selected.[69] The calculated eutectic coupled zone results are plotted in Figure 11(a) as a dashed line, solid line, and dash-dot line for dendrite Eqs. [1–3], respectively. All three calculated transition lines have a good fit to the experimental data at low growth velocities and hypoeutectic compositions. There is discrepancy between the calculations and experiments at higher velocities that need to be explored further, but all three calculated transition lines correctly capture the skew of the Sn–Ag coupled zone.

In the literature (*e.g.*, Reference 73), it is common to attribute the high fraction of $\beta$-Sn dendrites in near-eutectic Sn–Ag and Sn–Ag–Cu solders to the nucleation difficulties of the $\beta$-Sn phase which causes primary $Ag_3Sn$ and/or $Cu_6Sn_5$ to nucleate first and enrich the liquid in Sn as they grow so that, once $\beta$-Sn does nucleate, it grows in a liquid of higher Sn–content than $C_0$. Figure 11 confirms that there is additionally a growth competition between $\beta$-Sn dendrites and a $\beta$-Sn + $Ag_3Sn$ eutectic front which causes a transition to $\beta$-Sn dendrites at high growth velocity even in hypereutectic alloys without any primary $Ag_3Sn$.

### D. *$Ag_3Sn$ Particle Formation*

To explore the conditions required for $Ag_3Sn$ to develop into particles, the highest available pulling rate of 1000 $\mu m\ s^{-1}$ was imposed. At this velocity, all compositions grew with $\beta$-Sn dendrites ahead of the eutectic front (Figure 11(a)). Near-steady state growth at 1000 $\mu m\ s^{-1}$ resulted in $Ag_3Sn$ rods with undulations in their width but few or no $Ag_3Sn$ particles. A typical example of rods with perturbations/undulations is given in Figures 12(a) and (b).

It was found that rods with perturbations broke down into $Ag_3Sn$ particles when unsteady growth was imposed at high velocity. For example, Figures 12(c) through (d) show $Ag_3Sn$ rods breaking down into particles when the growth velocity abruptly increased from stationary to $V = 1000\ \mu m\ s^{-1}$. The initial long $Ag_3Sn$ rods broke up into short rods, and then into nanoscale round particles. In another example, Figures 12(e) and (f) show the

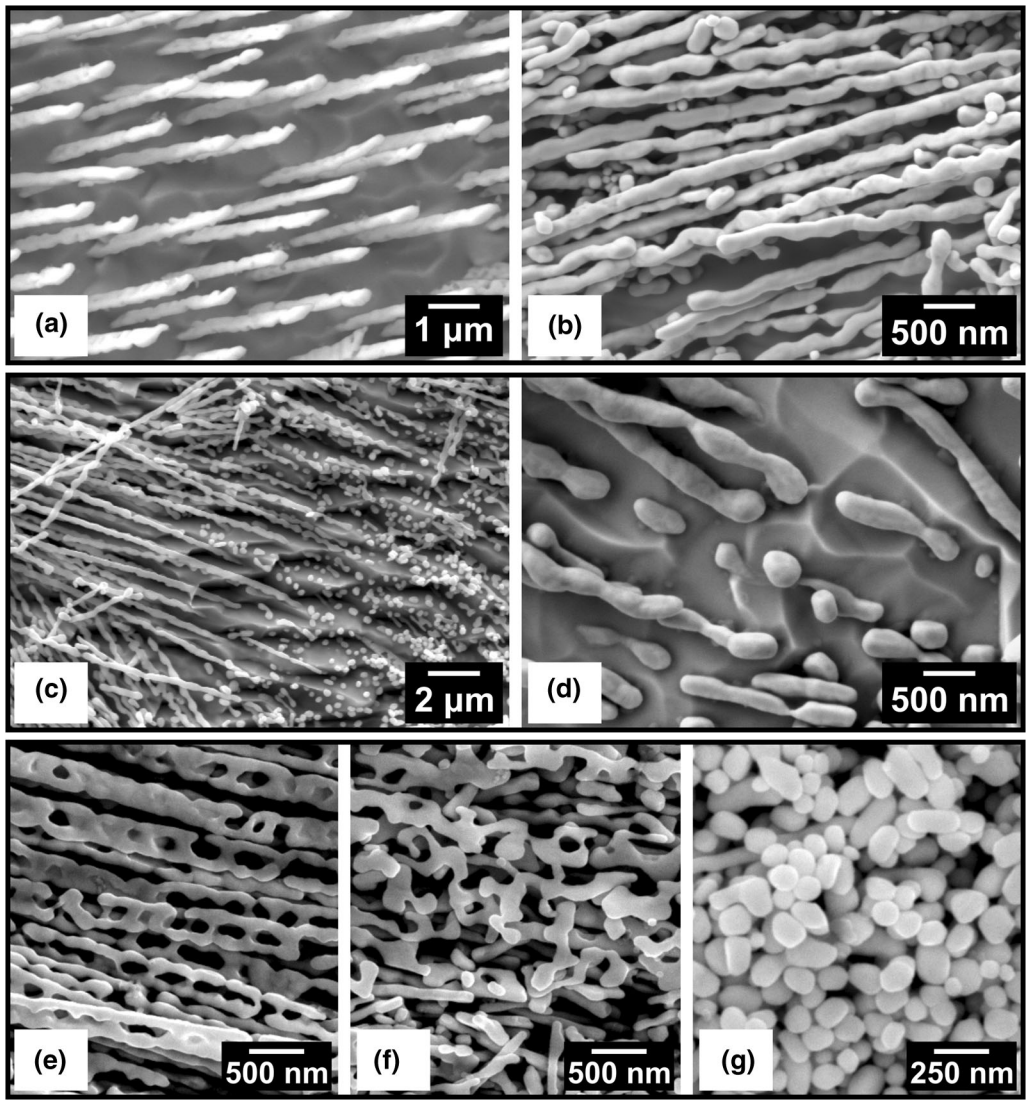


Fig. 12—(*a*) and (*b*) near-steady state growth of Sn–3.7Ag at 1000 $\mu$m s$^{-1}$ produced rods with perturbations. (*c*) through (*g*) unsteady growth of Sn–3.7Ag resulting in the break down of rods into particles. (c) through (d) after an abrupt increase from 0 to 1000 $\mu$m s$^{-1}$. (e) through (g) after an abrupt increase in heat extraction by gas-quenching a sample growing at 1000 $\mu$m s$^{-1}$.

morphology changes when a sample undergoing near-steady state growth at 1000 $\mu$m s$^{-1}$ experienced an abrupt increase in heat extraction *via* compressed-air gas cooling near the moving interface. The long $Ag_3Sn$ rods with perturbations initially developed into 'chain-like' rods with holes (Figure 12(e)), which then broke up into complex-shaped particles (Figure 12(f)) that, after some distance growing, developed into round nanoscale $Ag_3Sn$ particles (Figure 12(g)).

A separate series of experiments studied $Ag_3Sn$ rod pinch-off into particles in the solid state. Sn–3.7Ag was first grown at $V = 1000$ $\mu$m s$^{-1}$ and was then held stationary in the temperature gradient for some time. The initial $Ag_3Sn$ growth microstructure was aligned long rods with perturbations/undulations, similar to Figures 12(a) and (b). After 1 hour holding in Figures 13(a) and (b), some rods were starting to break up into short rods (Figure 13(a)) and some had developed into round particles (Figure 13(b)), producing a mixture of $Ag_3Sn$ short rods and round particles. After 18 hours holding, the $Ag_3Sn$ rods had fully developed into round particles (Figures 13(c) through (d)) that were coarser than those after 1 hours holding in (Figure 13(b)).

The development of perturbations on eutectic rods is related to Rayleigh instability where the pinch-off into particles reduces the interfacial area and, therefore, Gibbs energy. This is next explored in light of past work on eutectics for high temperature applications.[74–77] A pair of wavelength ($\lambda$), and average radius (a) were measured for 106 rods from three samples grown at 1000 $\mu$m s$^{-1}$ under near-steady state conditions, and the rod length was measured separately in lower magnification images. The ratio of rod length ($L_{rod}$) to the average rod diameter was $\frac{L_{rod}}{d} \gg 40$, which means the $Ag_3Sn$ rods can be assumed to be infinite fibers.[78] The ratio between wavelength and average radius was calculated and is plotted in Figure 14. Most rods had $\frac{\lambda}{a} \leq 8.9$ and one rod

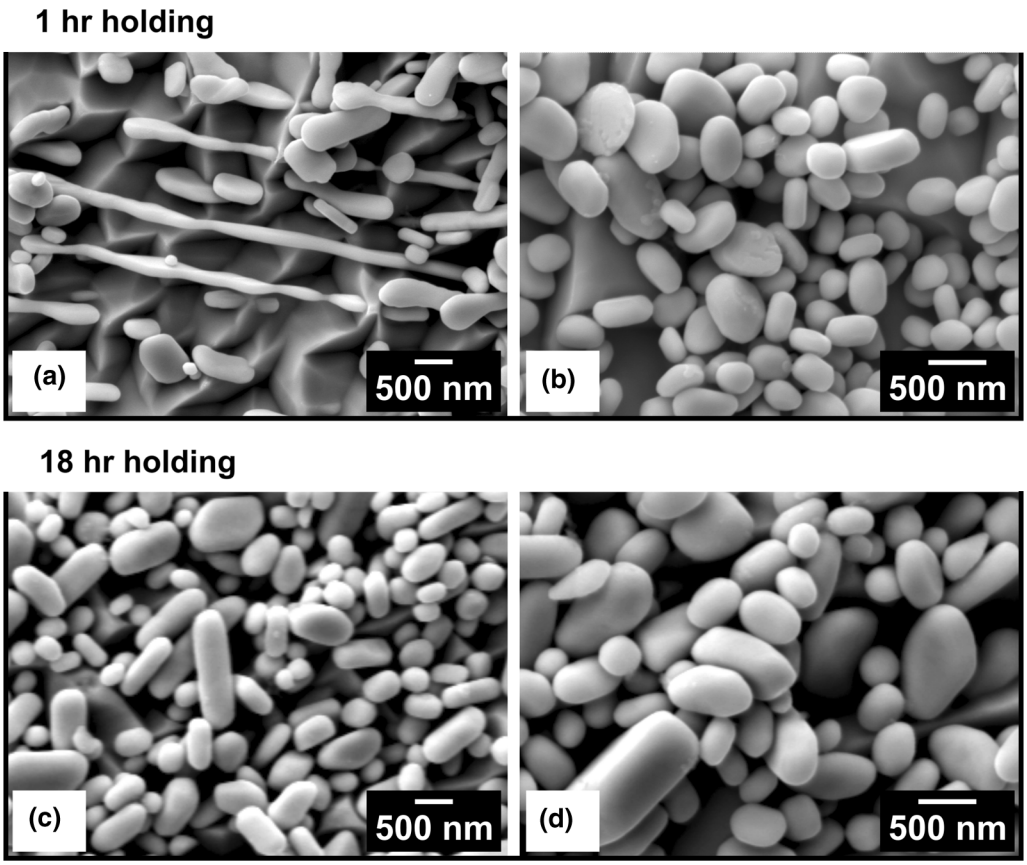


Fig. 13—Rod pinch-off into nanoscale particles during solid-state holding in a temperature gradient of 12 K/mm. (*a*) and (*b*) after 1 h holding. (*c*) and (*d*) after 18 h holding. Samples are Sn–3.7Ag previously grown at near-steady state at 1000 $\mu$m s$^{-1}$.

had $\frac{\lambda}{a} = 9.2$, and the fastest wavelength or maximum wavelength is about 9.2a. This suggests the pinch-off into particles is controlled by interface diffusion mechanisms, but further calculations would require values for the interface diffusivities between the $Ag_3Sn$ rod and $\beta$-Sn matrix.[74,78] 93 out of 106 cases had $\lambda < 2\pi a$ where the perturbation increases the energy of the configuration and is therefore unstable and decays.[78] 13 out of 106 cases had $\lambda > 2\pi a$ where there is a decrease in surface area and the perturbation is stable and will grow.[78] This is reasonable based on the rod shape in Figures 13(a) and (b); some rods have a large amplitude perturbation and some rods do not have perturbations (nearly flat rod edge surface). The results suggest that a Rayleigh instability is the main factor influencing necking-down and the pinching-off mechanisms in $Ag_3Sn$ rods.[75,77] It is also likely that both unsteady growth and solid-state pinch-off mechanisms are active. Past work has shown that growth faults including grain boundaries, branches, necking, *etc*. increase the kinetics of pinch-off.[75,77] This is also likely to be important in Sn–$Ag_3Sn$ but further TEM work is required to better understand growth faults within $Ag_3Sn$ rods.

The most common $Ag_3Sn$ morphology in Sn–Ag and Sn–Ag–Cu joints after electronic soldering is nanoscale $Ag_3Sn$ particles.[23–26,28] Comparing solder joints with this unidirectional solidification study, it can be seen that nanoscale $Ag_3Sn$ particles in joints could either form during unsteady growth at high velocity or by solid-state pinch-off after solidification, or both. High-velocity unsteady eutectic solidification is likely to occur in solder joints due to (i) the relatively deep nucleation undercooling required for the $\beta$-Sn phase (typically 20 to 40 K[73,79–81]) and (ii) multidirectional solidification with greater obstruction from surrounding $\beta$-Sn dendrites in a solder joint compared with aligned columnar dendrites in unidirectional solidification. It is also likely that solid-state pinch-off occurs in some joints after solidification depending on the cooling conditions at the end of soldering.

## IV. CONCLUSIONS

This work has revealed the following new insights into the transitions between $\beta$-Sn + $Ag_3Sn$ eutectic growth morphologies:

– The crystallography of faceted $Ag_3Sn$ growth was similar for each eutectic growth morphology: irregular plate, broken-lamellar, and rod. Plates had (001) as the largest facet, rods were flattened with (001) as the largest facet and $\langle 010 \rangle$ was the preferred $Ag_3Sn$ growth direction in all cases.

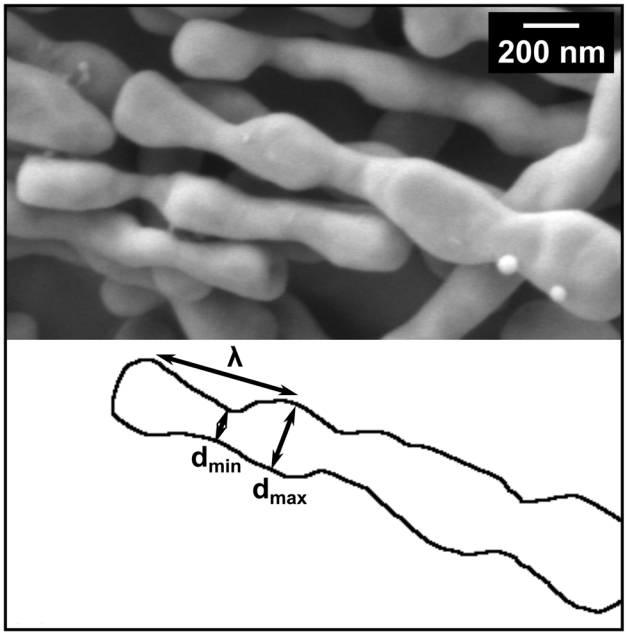


(a)

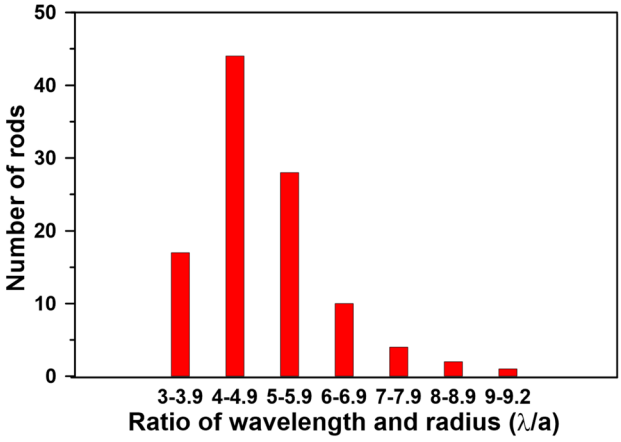


(b)

Fig. 14—Analysis of rod perturbations. (*a*) definitions of rod wavelength and maximum and minimum rod diameter. (*b*) Histogram of the ratio of wavelength to average radius in 106 measured rods grown at near-steady state at 1000 $\mu$m $s^{-1}$.

- Eutectic $\beta$-Sn grew with one orientation across the cross-section in the late stages of steady state growth with $\langle 100 \rangle_{Sn}$ or $\langle 110 \rangle_{Sn}$ close to the pulling direction.
- The transition from irregular plate to broken-lamellar morphology coincided with the transition from growth without a preferred $\beta$-Sn + $Ag_3Sn$ orientation relationship (OR) to the growth of a crystallographically locked eutectic where one of two ORs remained fixed during growth:

$$\text{OR 1}: (001)_{Ag_3Sn}//(301)_{Sn} \text{and} [010]Ag_3Sn\ //[010]Sn$$

$$\text{OR 2}: (001)_{Ag_3Sn}//(001)_{Sn} \text{and} [010]Ag_3Sn\ //[010]Sn$$

- The transition from broken-lamellar to rod morphology did not involve a change in the growth OR nor a change in the crystallographic growth direction or the main interface planes. Serrated edges on the sides of $Ag_3Sn$ lamellae grew off as branches, and the main (001) facet of lamellae became the facets of the flattened rods.
- The transition from fully eutectic growth to $\beta$-Sn dendrites ahead of a eutectic front could be reasonably calculated by a competitive growth criterion using measurements of the eutectic growth temperature and analytical models for the dendrite tip temperature. The presence of $\beta$-Sn dendrites disrupted subsequent eutectic growth and most samples containing $\beta$-Sn dendrites did not have a reproducible/simple eutectic OR.
- Nanoscale $Ag_3Sn$ particles formed during unsteady growth at 1000 $\mu$m $s^{-1}$ and during extended holding in a temperature gradient after growth at 1000 $\mu$m $s^{-1}$. In both cases, the mechanism was perturbations in the rod thickness and pinch-off by a Rayleigh-type instability.
- This research indicates that the nanoscale $Ag_3Sn$ particles common in electronic solder joints form during unsteady growth at high velocity and, under some conditions, by solid-state pinch-off mechanisms.

## ACKNOWLEDGMENTS

This work was partially funded by the UK EPSRC Grant EP/R018863/1. The authors acknowledge use of characterization facilities within the Harvey Flower Electron Microscopy Suite, Department of Materials, Imperial College London. Synchrotron experiments were performed on BL20XU at SPring-8 in Hyogo, Japan, under Grant Numbers 2015A1675 and 2020A1491. We thank MSc student Chung-Ting Fan for providing some Sn–4Ag datapoints in Figure 11(a).

## CONFLICT OF INTEREST

The authors declare no conflict of interest.

## OPEN ACCESS

## SUPPLEMENTARY INFORMATION

The online version contains supplementary material available at https://doi.org/10.1007/s11661-022-06937-2.

## REFERENCES


1. K. Suganuma, S.-H. Huh, K. Kim, H. Nakase, and Y. Nakamura: *Mater. Trans.*, 2001, vol. 42, pp. 286–91.
2. J. Keller, D. Baither, U. Wilke, and G. Schmitz: *Acta Mater.*, 2011, vol. 59, pp. 2731–41.
3. S.-K. Seo, S.K. Kang, D.-Y. Shih, and H.M. Lee: *J. Electron. Mater.*, 2009, vol. 38, pp. 257–65.
4. S. Terashima, Y. Kariya, T. Hosoi, and M. Tanaka: *J. Electron. Mater.*, 2003, vol. 32, pp. 1527–33.
5. R.J. Coyle, K. Sweatman, and B. Arfaei: *JOM*, 2015, vol. 67, pp. 2394–415.
6. R. Coyle, M. Reid, C. Ryan, R. Popowich, P. Read, D. Fleming, M. Collins, J. Punch, and I. Chatterji: in *2009 59th Electronic Components and Technology Conference*, IEEE, 2009, pp. 423–30.
7. S. Jun, Y.-C. Liu, Y.-J. Han, H. Gao, W.E.I. Chen, and Y.-Q. Yang: *Trans. Nonferrous Met. Soc. China*, 2006, vol. 16, pp. 59–64.
8. G. Wei and L. Wang: in *2012 13th International Conference on Electronic Packaging Technology & High Density Packaging*, IEEE, 2012, pp. 453–56.
9. F. Ochoa, J.J. Williams, and N. Chawla: *JOM*, 2003, vol. 55, pp. 56–60.
10. W.R. Osório, D.R. Leiva, L.C. Peixoto, L.R. Garcia, and A. Garcia: *J. Alloys Compd.*, 2013, vol. 562, pp. 194–204.
11. Y. Xu, T. Gu, J. Xian, F. Giuliani, T.B. Britton, C.M. Gourlay, and F.P.E. Dunne: *Int. J. Plast.*, 2021, vol. 137, p. 102904.
12. T. Gu, C.M. Gourlay, and T.B. Britton: *J. Electron. Mater.*, 2021, vol. 50, pp. 926–38.
13. A. Moore and R. Elliott: *Iron Steel Inst. Lond.*, 1968, vol. 15, pp. 167–72.
14. J.F. Bromley, F. Vnuk, and R.W. Smith: *J. Mater. Sci.*, 1983, vol. 18, pp. 3143–53.
15. H. Esaka, K. Shinozuka, and M. Tamura: *Mater. Trans.*, 2005, vol. 46, pp. 916–21.
16. M. Şahin and E. Çadirli: *J. Mater. Sci. Mater. Electron.*, 2012, vol. 23, pp. 484–92.
17. A. Moore: *The Solidification of Eutectic Alloys*, PhD thesis., The University of Manchester (United Kingdom), 1967.
18. L.R. Garcia, W.R. Osório, and A. Garcia: *Mater. Des.*, 2011, vol. 32, pp. 3008–12.
19. Thermo-Calc: 2015.
20. H. Esaka, M. Tsuji, M. Tamura, and K. Shinozuka: *Fourth Pacific Rim Int. Conf. Adv. Mater. Process.* (2001).
21. M.N. Croker, R.S. Fidler, and R.W. Smith: *Proc. R. Soc. London. A*, 1973, vol. 335, pp. 15–37.
22. L. Snugovsky, P. Snugovsky, D.D. Perovic, T. Sack, and J.W. Rutter: *Mater. Sci. Technol.*, 2005, vol. 21, pp. 53–60.
23. R.S. Sidhu, S.V. Madge, X. Deng, and N. Chawla: *J. Electron. Mater.*, 2007, vol. 36, pp. 1615–20.
24. B. Arfaei and E. Cotts: *J. Electron. Mater.*, 2009, vol. 38, pp. 2617–27.
25. F. Mutuku, B. Arfaei, and E.J. Cotts: *J. Electron. Mater.*, 2017, vol. 46, pp. 2067–79.
26. J.W. Xian, S.A. Belyakov, and C.M. Gourlay: *J. Electron. Mater.*, 2021, vol. 50, pp. 786–95.
27. R.S. Sidhu and N. Chawla: *Mater. Charact.*, 2004, vol. 52, pp. 225–30.
28. B.L. Silva, A. Garcia, and J.E. Spinelli: *Microelectron. Reliab.*, 2014, vol. 54, pp. 2929–34.
29. H.-T. Lee and Y.-F. Chen: *J. Alloys Compd.*, 2011, vol. 509, pp. 2510–17.
30. J. Shen, Y.C. Chan, and S.Y. Liu: *Intermetallics*, 2008, vol. 16, pp. 1142–148.
31. W. Kurz and D.J. Fisher: *Int. Met. Rev.*, 1979, vol. 24, pp. 177–204.
32. B. Toloui and A. Hellawell: *Acta Metall.*, 1976, vol. 24, pp. 565–73.
33. H. Yasuda, I. Ohnaka, K. Kawasaki, A. Sugiyama, T. Ohmichi, J. Iwane, and K. Umetani: *J. Cryst. Growth*, 2004, vol. 262, pp. 645–52.
34. N. Hou, S.A. Belyakov, L. Pay, A. Sugiyama, H. Yasuda, and C.M. Gourlay: *Acta Mater.*, 2018, vol. 149, pp. 119–31.
35. C.A. Schneider, W.S. Rasband, and K.W. Eliceiri: *Nat. Methods*, 2012, vol. 9, pp. 671–75.
36. V.T. Witusiewicz, U. Hecht, S. Rex, and M. Apel: *Acta Mater.*, 2005, vol. 53, pp. 3663–69.
37. M. Serefoglu and R.E. Napolitano: *Acta Mater.*, 2008, vol. 56, pp. 3862–873.
38. C.W. Fairhurst and J.B. Cohen: *Acta Crystallogr. Sect. B*, 1972, vol. 28, pp. 371–78.
39. E. Rönnebro, J. Yin, A. Kitano, M. Wada, and T. Sakai: *Solid State Ionics*, 2005, vol. 176, pp. 2749–57.
40. P.J. Rossi, N. Zotov, and E.J. Mittemeijer: *Zeitschrift für Krist. Mater.*, 2016, vol. 231, pp. 1–9.
41. M. Mueller, I. Panchenko, S. Wiese, and K.-J. Wolter: *IEEE Trans. Components Packag. Manuf. Technol.*, 2019, vol. 10, pp. 18–29.
42. H. Yu, Y. Sun, W.R. Meier, P.C. Canfield, C.R. Weinberger, S.-W. Lee, and M. Aindow: *J. Mater. Sci.*, 2018, vol. 53, pp. 5317–28.
43. H.E. Swanson: *Standard X-Ray Diffraction Powder Patterns*, vol. 1, US Department of Commerce, National Bureau of Standards, 1953.
44. S.C. Flood and J.D. Hunt: *Met. Sci.*, 1981, vol. 15, pp. 287–94.
45. M. Gündüz, H. Kaya, E. Çadırlı, and A. Özmen: *Mater. Sci. Eng. A*, 2004, vol. 369, pp. 215–29.
46. L.M. Hogan and H. Song: *Metall. Mater. Trans. A*, 1987, vol. 18, pp. 707–13.
47. P. Magnin and R. Trivedi: *Acta Metall. Mater.*, 1991, vol. 39, pp. 453–67.
48. D.J. Fisher and W. Kurz: *Acta Metall.*, 1980, vol. 28, pp. 777–94.
49. H. Jones and W. Kurz: *Int. J. Mater. Res.*, 1981, vol. 72, pp. 792–97.
50. P. Magnin and W. Kurz: *Acta Metall.*, 1987, vol. 35, pp. 1119–128.
51. U. Böyük and N. Maraşlı: *Mater. Chem. Phys.*, 2010, vol. 119, pp. 442–48.
52. R. Elliott: in *Eutectic Solidification Processing*, R. Elliott, ed., Butterworth-Heinemann, 1983, pp. 120–56.
53. M. Rappaz and J.A. Dantzig: *Solidification*, EPFL Press, Lausanne, 2009, pp. 386–415.
54. B. Caroli, C. Caroli, G. Faivre, and J. Mergy: *J. Cryst. Growth*, 1992, vol. 118, pp. 135–50.
55. S. Mohagheghi and M. Şerefoğlu: *Acta Mater.*, 2018, vol. 151, pp. 432–42.
56. S. Bottin-Rousseau, M. Medjkoune, O. Senninger, L. Carroz, R. Soucek, U. Hecht, and S. Akamatsu: *J. Cryst. Growth*, 2021, vol. 570, p. 126203.
57. Z.L. Ma, J.W. Xian, S.A. Belyakov, and C.M. Gourlay: *Acta Mater.*, 2018, vol. 150, pp. 281–94.
58. K.A. Jackson and J.D. Hunt: *AIME Met Soc Trans*, 1966, vol. 236, pp. 1129–42.
59. R.T. Southin and B.L. Jones: *The Micromorphology of High Volume-Ratio Eutectics: A Scanning Electron Microscope Study*, DTIC Document, 1968.
60. R. Yoshimura, K. Morishita, H. Yasuda, H. Esaka, and K. Shinozuka: *J. Jpn Inst. Met.*, 2018, vol. 82, pp. 78–83.
61. H. Esaka and W. Kurz: *J. Cryst. Growth*, 1984, vol. 69, pp. 362–66.

62. M. Rappaz and P. Thevoz: *Acta Metall.*, 1987, vol. 35, pp. 1487–97.
63. M. Rappaz and J.A. Dantzig: *Solidification*, EPFL Press, Lausanne, 2009.
64. G. Ivantsov: *Dokl. Akad. Nnuk.*, 1947, vol. 58, p. 567.
65. J. Lipton, M.E. Glicksman, and W. Kurz: *Mater. Sci. Eng.*, 1984, vol. 65, pp. 57–63.
66. J. Lipton, M. Glicksman, and W. Kurz: *Metall. Mater. Trans. A*, 1987, vol. 18, pp. 341–45.
67. H. Jones and W. Kurz: *Metall. Trans. A*, 1980, vol. 11, pp. 1265–73.
68. M.H. Burden and J.D. Hunt: *J. Cryst. Growth*, 1974, vol. 22, pp. 109–16.
69. M.H. Burden and J.D. Hunt: *J. Cryst. Growth*, 1974, vol. 22, pp. 328–30.
70. B. Saatçi, F. Meydaneri, M. Özdemir, E. Yılmaz, and A. Ülgen: *Surf. Sci.*, 2011, vol. 605, pp. 623–31.
71. J. Cahoon, Y. Jiao, K. Tandon, and M. Chaturvedi: *J. Phase Equilib. Diffus.*, 2006, vol. 27, pp. 325–32.
72. S. Engin, U. Böyük, and N. Maraşlı: *J. Alloys Compd.*, 2009, vol. 488, pp. 138–43.
73. D. Swenson: *Lead-Free Electronic Solders*, Springer, New York, 2006, pp. 39–54.
74. D.R.H. Jones: *J. Mater. Sci.*, 1974, vol. 9, pp. 989–92.
75. D.R.H. Jones, I.R. Sare, W.J. Morgan, and D.S.O. Tinn: *J. Mater. Sci.*, 1976, vol. 11, pp. 855–58.
76. I.R. Hughes and H. Jones: *J. Mater. Sci.*, 1976, vol. 11, pp. 1781–93.
77. Y.G. Nakagawa and G.C. Weatherly: *Acta Metall.*, 1972, vol. 20, pp. 345–50.
78. M. McLean: *Directionally Solidified Materials for High Temperature Service*, 1988.
79. B. Arfaei, M. Benedict, and E.J. Cotts: *J. Appl. Phys.*, 2013, vol. 114, p. 173506.
80. G. Parks, A. Faucett, C. Fox, J. Smith, and E. Cotts: *JOM*, 2014, vol. 66, pp. 2311–19.
81. C.M. Gourlay, S.A. Belyakov, Z.L. Ma, and J.W. Xian: *JOM*, 2015, vol. 67, pp. 2383–93.